Volume 1 | Number 1 | Jan 2013 | Pages 1–100

Journal of
Materials Chemistry C

Materials for optical and electronic devices
www.rsc.org/materialsC

ROYAL SOCIETY
OF CHEMISTRY

ROYAL SOCIETY
OF CHEMISTRY

www.rsc.org/materialsC

J. Mater Chem

ARTICLE TYPE

Di-amidosils with Tunable Structure, Morphology and Emission Quantum Yield: The Role of Hydrogen Bonding.

S. C. Nunes,[a,b]* J. Hümmer,[b] V. T. Freitas,[c] R. A. S. Ferreira,[c] L. D. Carlos,[c] P. Almeida,[a] V. de Zea Bermudez[b,d]*

Tailoring of the structure (from amorphous to highly ordered lamellar), morphology (from a homogenous texture to fibers, microparticles, seaweeds- and desert rose-like shapes) and photoluminescence features of five di-amide crossed-linked decyl/siloxanes (di-amidosils, d-A(10)) was achieved via sol-gel chemistry and self-assembly from a single precursor through a fine control of the reaction conditions (water content, catalyst presence/type (HCl or NaOH)/concentration and co-solvent presence/type (ethanol or DMSO)). All the hybrids analyzed are multi-wavelength emitters under UV/VIS excitation. Irrespective of the degree of order of the materials, the highest emission quantum yield values (ca. 013 ± 0.01 at λ_{exc} = 400 nm) were found in samples synthesized in the presence of a catalyst. Comparison of the present data with those reported by our group for a shorter chain di-amidosil and for mono-amidosils revealed that in the amidosils the emission quantum yield is intimately associated with the degree of order of the amide-amide hydrogen-bonded network. This enabled us to establish for the first time a rational and straightforward way of predicting *grosso modo* the magnitude of the emission quantum yield of an amidosil hybrid prior to measurements, which requires simply the analysis of the amide I band of the FT-IR spectrum. This correlation opens the way to exciting new prospects for the design of new luminescent organic/inorganic hybrids with enhanced properties.

Introduction

Inspired by Nature, the self-assembly of organic/inorganic hybrid materials[1,2] provides an adequate approach for the production of complex hierarchical architectures[3,4] and multifunctional nanostructures for numerous technological applications.[2,5,6,7]

The combined use of sol-gel chemistry[8] with self-assembly processes[9] has been the preferred route to prepare silica-based hybrid materials with well-ordered structures.[10-12] Long-range ordered organic/inorganic hybrids can be essentially prepared by means of two synthetic pathways: (a) In the presence of templates (usually surfactants);[11-16] (b) In the absence of templates and using monomers bearing organic groups prone to participating in hydrophobic interactions (weak van der Waals forces),[17-26] $\pi-\pi$ interactions[27-29] or hydrogen bonding interactions.[21-23,25-27,29] The degree of order of the resulting materials may be easily tuned by subtle modifications of the synthetic conditions and through a judicious choice of the chemical nature of the organic and inorganic components.

Bridged silsesquioxane (BS) structures have been extensively investigated in this context.[21-26] Typically they are prepared in an acidic solution from organobridged trialkoxysilane precursors $(RO)_3Si-Y-R'-Y-Si(OR)_3$ (where R' is an alkyl chain with variable length, an aryl group or a cyclohexylene group, and Y is a self-associating moiety) yielding organized materials with a wide variety of well-organized morphologies (lamellar structures,[21,23-26] helical fibers,[30] spheres or hollow tubes[22]).

The most extensively studied ordered BSs have been the lamellar packed structures produced via acid-catalyzed hydrolysis in a large excess of water of the alkyl-based precursors $(CH_3CH_2O)_3-Si-(CH_2)_m-U-(CH_2)_n-U-(CH_2)_m-Si-(OCH_2CH_3)_3$ (where m = 3 and U is the urea (-NHC(=O)NH-) group) (**Pn**). In these hybrids the degree of order increases with the length of the central spacer. Chains n < 8 yielded, however, disordered materials, regardless of the reaction conditions employed.[26] Amorphous materials resulted from F⁻-catalyzed hydrolysis under stoichiometric conditions of same precursors.[23] The lamellar BSs derived from precursors with n = 7, 9-12, m = 10 and U = urea group (**P10-n-10**) demonstrated that the length of the side spacers plays a unique role in the structuring of alkyl-based BS.[26]

In 2005 we developed novel BSs from the organobridged trialkoxysilane precursors $(CH_3CH_2O)_3Si-(CH_2)_3-A-(CH_2)_n-A-(CH_2)_3-Si(OCH_2CH_3)_3$ (where n = 4 and 8 and A is the amide (-NHC(=O)-) group) using classical sol-gel reactions.[31] These di-amide cross-linked alkyl/siloxane xerogels, designated as di-amidosils and represented by the notation d-A(n) (where d

represents di), were produced as transparent, amorphous and rigid monoliths.[31] With the primary goal of reversing the natural tendency of the d-A(10) di-amidosil to become disordered, we have synthesized in the present work the same material using different approaches. With this purpose, we have employed, not only the classical conditions of the sol-gel process, but also acid- and base-catalyzed hydrolytic sol-gel methods in combination with self-assembly routes. In the case of the acid-catalyzed synthesis, we have further studied the influence of the presence and nature of a co-solvent. The structure, morphology and photoluminescente features of these di-amidosil samples have been studied in-depth. The ultimate goal of this work has been to get insight into the factors responsible for the different emission quantum yield values exhibited by these amide cross-linked hybrids (and analogues) and in particular to elucidate the exact role of hydrogen bonding interactions in this context.

Experimental Section

Material

Pyridine (py, Panreac, 99.8 %), and tetrahydrofuran (THF, Aldrich-Sigma, 99.9 %) were stored over molecular sieves. (3-aminopropyl)triethoxysilane ($(CH_3CH_2O)_3Si(CH_2)_3NH_2$, APTES, Aldrich, 99 %), dodecanedioyl dichloride ($ClC(=O)-(CH_2)_{10}C(=O)Cl$, DdC, Aldrich, 98 %), dimethyl sulfoxide (DMSO, Riedel-de Haën, dried max. 0.03 % H_2O), hydrochloric acid (HCl, 37 %, Pronalab), sodium hydroxide (NaOH, Sigma-Aldrich, 99.99 %) and ethanol (CH_3CH_2OH, Fábrica de Álcool – Manuel Vieira e Ca. (Irmão) Sucrs. Lda, 99.9 %) were used as received. Amberlyst A-21 Ion-Exchange Resin (4.7 meq/g, Aldrich) was washed with THF and stored in an oven at 80 ºC. High purity deionized water (H_2O) (type II pure water, using Elix Reference Water Purification System 10 from Millipore) was used in all experiments.

Methods

The ^1H and ^{13}C Nuclear Magnetic Resonance (NMR) spectra were recorded in deuterated chloroform ($CDCl_3$) on a Bruker Avance III spectrometer (400 MHz) equipped with a TXI probe-head with inverse detection. Chemical shifts (δ) are reported in parts per million (ppm) relative to tetramethylsilane (TMS) and splitting multiplicities are described as s = singlet; t = triplet; or m = multiplet. Coupling constants (J values) are reported in Hertz (Hz).

^{29}Si Magic Angle Spinning (MAS) and ^{13}C Cross Polarization (CP)/MAS NMR spectra were recorded on a Bruker Avance 400 (9.4 T) spectrometer at 79.49 and 100.62 MHz, respectively. ^{13}C CP/MAS NMR spectra were recorded with 4 µs 1H 90º pulse, 2 ms contact time, a recycle delay of 4 s and at a spinning rate of 8 kHz. ^{29}Si MAS NMR spectra were recorded with 2 µs ($\theta \approx 30$ º) rf pulses, and recycle delay of 60 s and at a 5.0 kHz spinning rate. The δ are quoted in ppm from TMS.

The X-ray diffraction (XRD) patterns were recorded with a Philips X'Pert MPD powder X-ray diffractometer, using monochromated CuK_α radiation (λ=1.54 Å) over a scattering vector, q (q=4π sinθ/λ, 2θ being the scattering angle) range between 0.77 and 25 nm^{-1}.

Differential Scanning Calorimetry (DSC) measurements were obtained with a DSC 204 Netz sch. A mass of 2-5 mg was placed in 40 µL aluminum cans and stored in a desiccator over phosphorous pentoxide (P_2O_5) for one week at room temperature under vacuum. After the drying treatment the can was hermetically sealed and the thermogram was recorded. Each sample was heated from 20 to 140 ºC at 10 ºC min^{-1}. The purge gas used in all experiments was high purity nitrogen (N_2) supplied at a constant 25 cm^3 min^{-1} flow rate.

Scanning electron microscopy (SEM) images were obtained at 20 kV on a Hitachi Field Emission S-2700 microscope at low vacuum. Samples were first coated with gold (Au). SEM images were also obtained with a JEOL JSM 35C/Noran Voyager instrument (CEMUP-Porto contracts REEQ/1062/CTM/2005 and REDE/1512/RME/2005 FCT). Before analysis, the samples were coated with Au/palladium (Pd).

Transmission Electron Microscopy (TEM) images were obtained using a Hitachi HT7700. Solid particles were dispersed in ethanol using sonication, subsequently deposited on formval-coated copper grid (200 mesh) and then dried in air prior to analysis.

Atomic Force Microscopy (AFM) images were recorded in a Veeco Metrology Multimode/Nanoscope IVA equipment (CEMUP-Porto contract REEQ/1062/CTM/2005), in tapping mode using a super sharp silicon tip, curvature radius 10 nm, and frequency resonance equals to ≈300 KHz. Flattening and elimination of line noise tools and a Lowpass filter provided by the WSXM software[32] were used to improve the quality of the images.

Attenuated Total Reflectance (ATR) Fourier Transform Infrared (FT-IR) spectra were collected on a Thermoscientific Nicolet iS10: smart iTR, equipped with a diamond ATR crystal. For ATR data acquisition, approximately 1 mg of the sample was placed onto the crystal and the spectrum was recorded. An air spectrum was used as reference in absorbance calculations. The sample spectra were collected at room temperature in the 4000-400 cm^{-1} range by averaging 64 scans at a spectral resolution of 4 cm^{-1}.

The Fourier Transform Raman (FT-Raman) spectra were recorded at room temperature with a Bruker Spectrometer, Model RFS100/S and the laser radiation emitted by the Nd:YAG with wavelenght at 1064 nm. The spectra were collected over 4000-500 cm^{-1} at a resolution of 4 cm^{-1}, 400 scans (about 20 min) and 300 mW (laser power).

To evaluate complex band FT-IR and FT-Raman envelopes and to identify underlying spectral components, the iterative least-squares curve-fitting procedure in the PeakFit software (version 4)[33] was used extensively throughout this study. The best fit of the experimental data was obtained by varying the frequency, bandwidth and intensity of the bands. Because of the morphology of materials under investigation, we employed Gaussian band functions in the case of the d-A(10) and BC-d-A(10) samples and Voight band functions in the case of the AC-d-A(10) di-amidosils.

The photoluminescence spectra were recorded at room temperature and at 12K with a modular double grating excitation spectrofluorimeter with a TRIAX 320 emission monochromator (Fluorolog-3, Horiba Scientific) coupled to a R928 Hamamatsu photomultiplier, using a front face acquisition mode. The excitation source was a 450 W Xe arc lamp. The emission spectra were corrected for detection and optical spectral response of the spectrofluorimeter and the excitation spectra were corrected for

J. Mater Chem

ARTICLE TYPE

the spectral distribution of the lamp intensity using a photodiode reference detector. The emission decay curves were measured with the setup described for the luminescence spectra using a pulsed Xe–Hg lamp (6 µs pulse at half width and 20–30 µs tail).

The absolute emission quantum yield values were measured at room temperature using a quantum yield measurement system C9920-02 from Hamamatsu. This system consists of a Xe arc lamp (150 W), a monochromator (bandwidth 2 nm, an integrating sphere made of Spectralon® (99% reflectance for wavelengths within 350-1650 nm) with inner diameter of 84 mm and a multichannel detector (wavelength resolution < 2 nm). The emission quantum yield (ϕ) is given by

$$\phi = \frac{N_{Emi}}{N_{Abs}} = \frac{\int_{\lambda_1}^{\lambda_2} \frac{\lambda}{hc}\left[I_{em}^{sample}(\lambda) - I_{em}^{reference}(\lambda)\right]d\lambda}{\int_{\lambda_3}^{\lambda_4} \frac{\lambda}{hc}\left[I_{ex}^{sample}(\lambda) - I_{ex}^{reference}(\lambda)\right]d\lambda} \quad (1)$$

where N_{Abs} and N_{Em} are the number of photons absorbed and emitted by a sample, respectively, h is Planck's constant, c is the velocity of light, I_{em}^{sample} and $I_{em}^{reference}$ are the emission intensities of the measured with and without a sample respectively, in the emission spectra wavelength interval $[\lambda_1,\lambda_2]$ and I_{ex}^{sample} and $I_{ex}^{reference}$ are the integrated intensities of the excitation radiation measured with and without a sample respectively, in the excitation wavelength interval $[\lambda_3,\lambda_4]$. In order to validate the calculation methodology, the emission quantum yield of a 1 mm thick pellet of the white standard sodium salicylate (Merck P.A.) was also measured under the same experimental conditions. The emission quantum yield value measured for sodium salicylate was 0.56 excited at 360 nm. The reproducibility of the measurement was tested by performing three measurements for each sample revealing a standard deviation below 0.5 %. The measurement accuracy is within 10% according to the manufacturer.
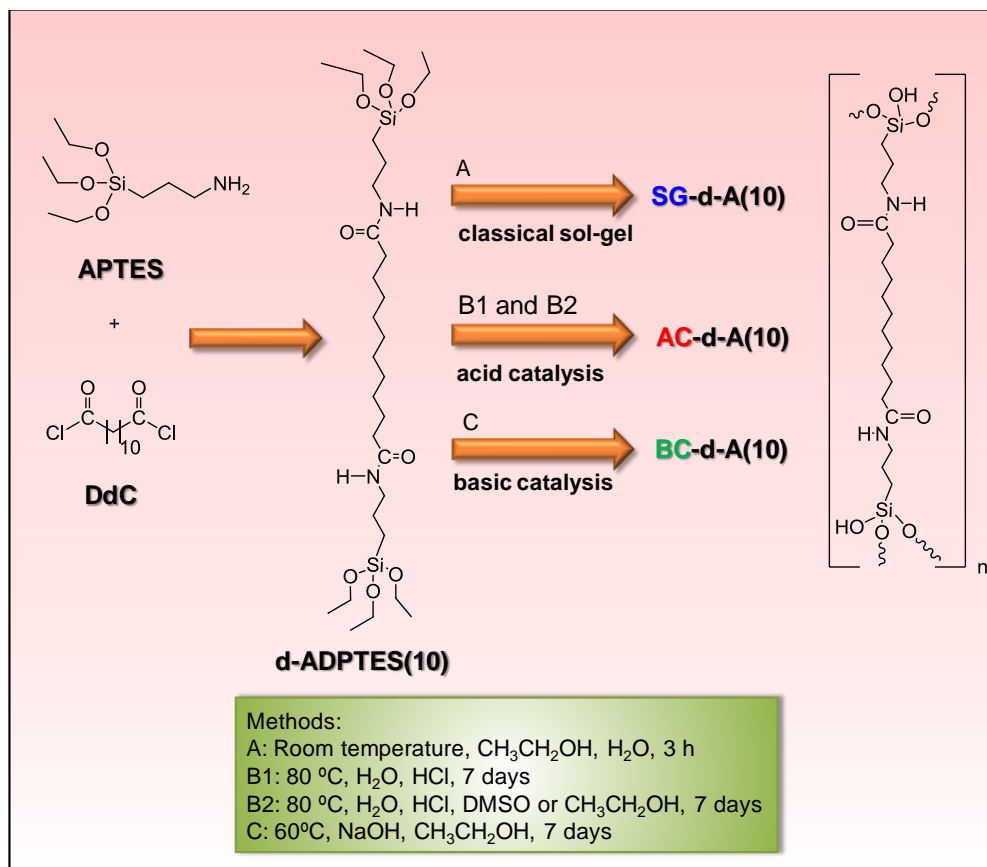
Synthesis

Synthesis of the di-amidosil precursor d-ADPTES(10) (Scheme 1). To synthesize the di-amidepropyltriethoxysilane (d-ADPTES(10)) precursor a volume (1 mL; 3.9 mmol) of DdC was added to a solution prepared through the addition of APTES (1.853 mL; 7.8 mmol) to 20 mL of THF solution containing py (127 mL; 1.56 mmol) and Amberlyst A-21 Ion-Exchange Resin (2.043 g; 9.4 mmol) (molar ratio APTES : DdC : py : resin = 2:1:0.4:2.4) (Scheme 1) and the mixture was stirred during one day. The intensity of the FT-IR band attributed to the stretching vibration of the C=O group of DdC, at approximately 1800 cm⁻¹ was progressively reduced, until it disappeared upon completion of the reaction. In parallel, a series of new bands, associated with the vibrations of the amide group, appeared in the 1760-1530 cm⁻¹ region. The solution was filtered and the solvent evaporated. The d-ADPTES(10) precursor, obtained as yellow oil, was dried under

vacuum for several hours. After drying under vacuum the precursor was obtained as an oil: Yield: 89 %; IR in cm⁻¹ (oil precursor):[21-23,31] 3278 (νNH), 2925 (ν_aCH₂), 2853 (ν_sCH₂), 1732 (νC=O), 1641 (νC=O) and 1547 cm⁻¹ (δNH); ¹H NMR (400 MHz, CDCl₃, TMS): δ = 0.61-0.57 (t, 4H; J = 8.0 Hz, C*H₂*Si), 1.23-1.01 (m, 30H, C*H₃* and C*H₂* (alkyl chain)), 1.62-1.54 (m, 8H, SiCH₂C*H₂* and C*H₂* (alkyl chain)), 2.13-2.09 (t, 4H, J = 8.0 Hz, COC*H₂*), 3.23-2.97 (m, 4H, NC*H₂*), 3.87-3.59 (m, 12H; SiOC*H₂*), 5.94 ppm (s, 2H; N*H*); ¹³C NMR (400 MHz, CDCl₃, TMS): δ = 7.40 (*C*H₂Si), 17.8 (*C*H₃), 22.5 (*C*H₂), 24.62 (SiCH₂*C*H₂), 28.98 (*C*H₂), 36.38 (C(=O)*C*H₂), 41.47 (N*C*H₂), 57.96 (*C*H₂OSi), 172 ppm (*C*O).

Synthesis of d-A(10) via classical sol-gel reactions. Method A in Scheme 1: A mixture of CH₃CH₂OH (1.866 mL) and H₂O (288 mL) (molar ratio APTES:H₂O: CH₃CH₂OH =1:2:4) was added to d-ADPTES(10) to promote the hydrolysis and condensation reactions characteristic of the sol-gel process. The di-amide alkyl/siloxane hybrid d-A(10) was obtained as a transparent, rigid monolith with a yellowish hue. This di-amidosil sample was identified using the notation SG-d-A(10), where SG stands for sol-gel process.

Synthesis of d-A(10) via acid-catalyzed hydrolysis of d-ADPTES(10) in a large excess of water. Method B1 in Scheme 1: H₂O and HCl (1M) were added to approximately 1 g of d-ADPTES(10). Different acid molar ratios d-ADPTES(10):H₂O:HCl=1:600:x were prepared (Table S1). The oily mixture was stirred at room temperature and after some minutes a white precipitate appeared. The mixture was then stirred in an oil-bath (80 ºC) for some minutes and was left standing during 1 week at the same temperature. The resulting white slurry solution was filtered and washed with H₂O until neutral pH was attained and again washed with CH₃CH₂OH and acetone. The white solid was dried at 50 ºC during 1 day. **Method B2 in Scheme 1:** The influence of a co-solvent on the structuring of selected samples was also examined. DMSO and CH₃CH₂OH were used for this purpose (Table S1). In such cases the precursor was dissolved in the co-solvent prior to the addition of H₂O and HCl. The addition of the co-solvents did not affect the pH. The acid-catalyzed di-amidosil samples were identified using the notation AC-d-A(10)(600:x:σ(solvent)), where AC stands for acid-catalyzed and σ represents the molar ratio of co-solvent per d-ADPTES(10) precursor.

Synthesis of d-A(10) via base-catalyzed hydrolysis of d-ADPTES(10). Method C in Scheme 1: Approximately 1 g of d-ADPTES(10) was dissolved in CH₃CH₂OH (3 mL). A volume of H₂O (7.5 mL) was then added yielding a white suspension. After adjusting the pH of the resulting solution to 12 through the addition of an aqueous solution of NaOH the white solution became an oily mixture (molar ratio APTES:H₂O:CH₃CH₂OH:NaOH=1:38.9:0.3:0.2). The latter was heated to 60 ºC under static conditions for 1 week (Table S1).

Scheme 1 Synthetic procedure of the d-A(10)-based di-amidosils

After a few days in static conditions a white crystalline solid was formed. After filtration, the solid was washed successively with water, ethanol and acetone. The base-catalyzed di-amidosil sample was identified using the notation BC-d-A(10), where BC stands for base-catalyzed.

Results and discussion

The most prominent peak in the ^{13}C CP/MAS spectra of SG-d-A(10), BC-d-A(10), AC-d-A(10) (600:0.2:100(ethanol)) and AC-d-A(10) (600:0.2:179(DMSO)) located at 30 ppm (Figures 1A(a), 1A(b), 1A(d) and 1A(e), respectively, and Table 1) indicates that in these samples most of the alkyl chains adopt *gauche* conformations.[34,35] In the ^{13}C CP/MAS spectrum of the AC-d-A(10) (600:0.2:0) di-amidosil two peaks are observed around 33 and 30 ppm (Figure 1A(c), Scheme 1 and Table 1) with practically the same intensity, suggesting that the proportion of all-*trans* and *gauche* conformers[34,35] is very similar. In contrast, the ^{13}C CP/MAS spectrum of AC-d-A(10) (600:1:0) is dominated by a peak at ca. 33 ppm (Figure 1A(f) and Table 1, pointing out that the great majority of the alkyl chains assume all-trans, highlyordered zig-zag conformations.[34-36] The presence of the resonances characteristic of the propyl chains and of the amide cross-links in the ^{13}C CP/MAS spectra of all the di-amidosils analysed (Figure 1A and Table 1) confirms that no cleavage of the functional groups occurred regardless of the synthesis conditions

employed. The absence of signals near 18 and 58 ppm in all the ^{13}C CP/MAS spectra (Figure 1A and Table 1) demonstrates that the hydrolysis of the Si-OCH$_2$CH$_3$ groups was complete.

The ^{29}Si MAS RMN spectrum of SG-d-A(10) exhibits two broad signals at ca. -58.7 and -67.3 ppm with similar intensity (Figure 1B(a) and Table 1) which are ascribed to T^2 [R-Si-(OSi)$_2$(OH)] and T^3 [R-Si(OSi)$_3$] (T^n is the conventional silicon notation[31,37] with n = 1, 2 and 3, n being the number of Si-bridging oxygen atoms) sites, respectively. In the case of BC-d-A(10), AC-d-A(10)(600:0.2:100(ethanol)), and AC-d-A(10) (600:0.2:179(DMSO)) the dominant signal of the ^{29}Si MAS NMR spectra, at -67.4, -66.2 and -65.8 ppm, respectively (Figures 1B(b), 1B(d) and 1B(e)), respectively), is associated with T^3 environments (Table 1). Out of these three ^{29}Si MAS RMN spectra, AC-d-A(10) (600:0.2:179(DMSO)) is the only one that exhibits T^1 ((R- Si(OSi)(OH)$_2$)) sites (Table 1). In contrast, the most intense feature of the ^{29}Si MAS NMR spectra of AC-d-A(10) (600:0.2:0) and AC-d-A(10) (600:1:0), centred at -57.5 and -57.8 ppm, respectively (Figures 1B(c) and 1B(f), respectively), is associated with T^2 sites (Table 1). In the latter two samples T^1 and T^3 environments are, however, also present (Figures 1B(c) and 1B(f), respectively). The absence of Q-type signals corresponding to SiO$_{4/2}$ units in the -90 to -120 ppm range of the ^{29}Si MAS NMR spectra of these samples (Figure 1B) confirms the integrity of the C-Si bonds during the synthesis (Table 1). The magnitude of the
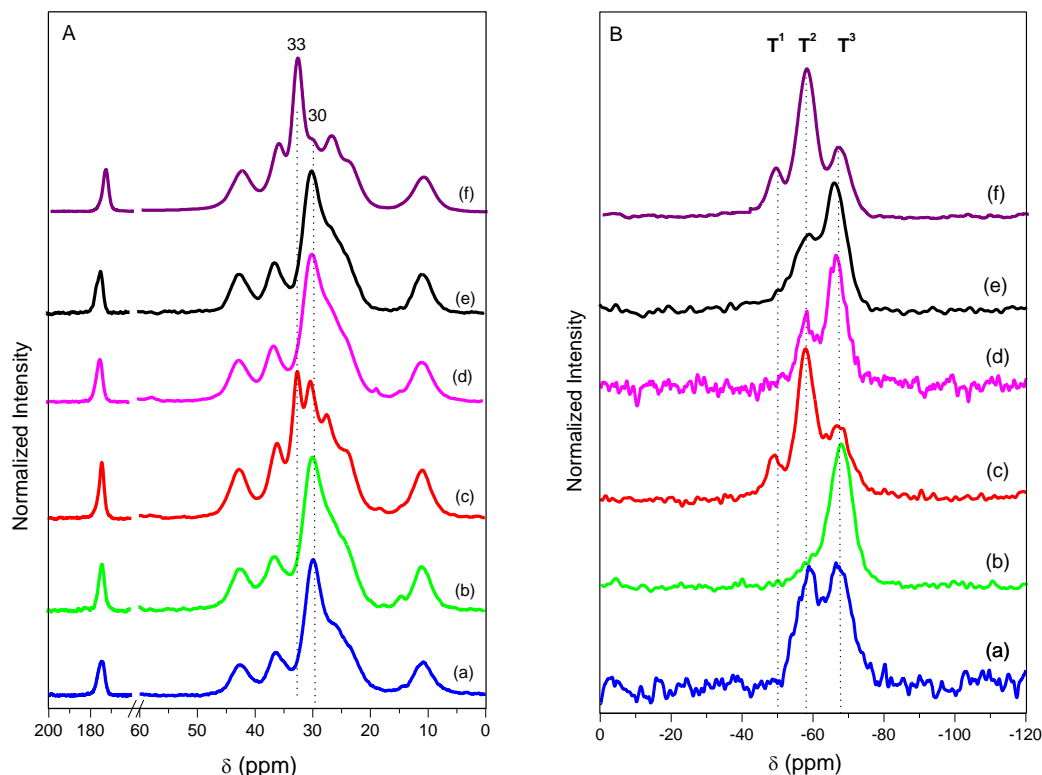
J. Mater Chem

ARTICLE TYPE

Figure 1 ^{13}C CP (A) and ^{29}Si (B) MAS NMR spectra of SG-d-A(10) (a), BC-d-A(10) (b), AC-d-A(10) (600:0.2:0) (c), AC-d-A(10) (600:0.2:100(ethanol)) (d), AC-d-A(10) (600:0.2:179(DMSO)) (e) and AC-d-A(10) (600:1:0) (f) di-amidosils.

polycondensation degree (*c*) calculated for AC-d-A(10) (600:0.2:0) and AC-d-A(10) (600:1:0) (74 and 72 %, respectively, Table 1) indicates that the addition of an acid catalyst and a large excess of water favoured the occurrence of a 2D siloxane network. These values are considerably lower than those of SG-d-A(10) (85 %), AC-d-A(10) (600:0.2:179(DMSO)) (87 %), AC-d-A(10) (600:0.2:100(ethanol)) (91 %) and BC-d-A(10) (96 %) (Table 1). Thus, while the incorporation of a basic catalyst into the reaction medium resulted in the formation of a truly 3D siloxane network,[38] the synthesis of AC-d-A(10) (600:0.2) in a large excess of DMSO (AC-d-A(10) (600:0.2:179(DMSO)) yielded a material with a *c* value that matches that of the sample SG-d-A(10), obtained under the classical sol-gel conditions.
The XRD patterns of SG-d-A(10), AC-d-A(10) (600:0.2:100(ethanol)), AC-d-A(10) (600:0.2:179(DMSO)) and BC-d-A(10) (Figures 2A(a), 2A(b), 2A(c) and 2A(d), respectively) indicate that these compounds are totally amorphous. The broad non-resolved band, Gaussian in shape, at ca 14.7 nm^{-1} (d_{Si} = 0.43 nm) is due to the coherent diffracting domains of the siliceous backbone.[39] These samples also give to a

peak at 3.3 nm^{-1} which corresponds to an interparticle distance d_{ip} = 2.0 nm.[31]
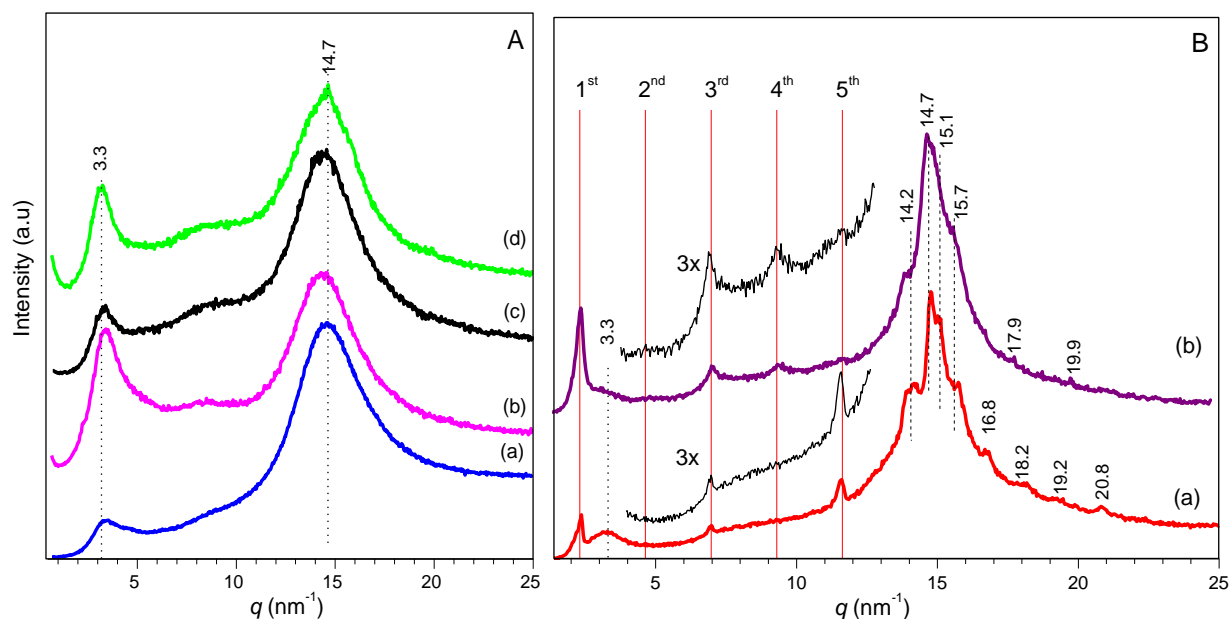
Structurally the AC-d-A(10) (600:0.2:0) and AC-d-A(10) (600:1:0) di-amidosils (Figures 2B(a) and 2B(b), respectively) differ markedly from the above mentioned samples (Figure 2A).

In the low-*q* region of the XRD patterns the acid-catalyzed samples AC-d-A(10) (600:0.2:0) and AC-d-A(10) (600:1:0) give rise to a peak at 2.3 nm^{-1} which corresponds to the first of the kth-order peaks (vertical red lines in Figure 2B) of a lamellar structure with spacing l = 2.71 nm (where $l = 2\pi/q_n$, with *q* representing the scattering vector). This value coincides with the length of the organic spacer deduced from ChemBioOffice software (Molecular modelling per formed with the MM2 model of ChemBio3D Ultra 2007, version 11.01). In the XRD pattern of AC-d-A(10) (600:1:0) the 1st peak is intense and sharp and the 3rd and 4th orders are clearly discerned (Figure 2B(b)). In the case of AC-d-A(10) (600:0.2:0) the 5th order reflection is distinctly seen, the 1st and 3rd peaks are weak and the 4th order is not detected (Figure

ARTICLE TYPE www.rsc.org/xxxxxx | XXXXXXXX

Table 1. ^{13}C CP/MAS and ^{29}Si MAS NMR data (δ in ppm) of selected di-amidosils. Notes: c (polycondensation degree) = $1/3[A(T^1)+2A(T^2)+3A(T^3)]*100$, A is the integral area in % and $R' \equiv NHC(=O)-(CH_2)_{10}-C(=O)NH$.

| [13]C CP/MAS					
AC-d-A(10) (600:x: σ (solvent))				BC-d-A(10)	Attribution[31,34-36]
600:0.2:0	600:1:0	600:0.2:179(DMSO)	600:0.2:100(ethanol)		
174	173	174	174	174	C=O
42	42	42	42	42	H_2CNH
36	36	36	36	36	$(C=O)CH_2$
33	33	-	-	-	CH_2 all-*trans* (alkyl chain)
30	-	30	30	30	CH_2 *gauche* (alkyl chain)
27	27	sh	sh	25, sh	CH_2 (alkyl chain)
24	23	sh	sh		$SiCH_2CH_2$
11	11	11	11	11	$SiCH_2$

[29]Si MAS[31,37]					
Sample	T^1 (A)	T^2 (A)	T^3 (A)	c	Empirical Formula
SG-d-A(10)	-	-58.7 (43.7)	67.3 (56.3)	85	$R'_{0.5}Si(OH)_{0.40}(O)_{1.1}$
AC-d-A(10) (600:0.2:0)	-49.0 (11.5)	-57.8 (54.1)	-66.6 (34.4)	74	$R'_{0.5}Si(OH)_{0.40}(O)_{1.1}$
(600:1:0)	-49.0 (11.8)	-57.5 (59.6)	-66.6 (28.6)	72	$R'_{0.5}Si(OH)_{0.40}(O)_{1.1}$
(600:0.2:179(DMSO))	-51.0 (3.9)	-58.2 (29.2)	-65.8 (66.8)	87	$R'_{0.5}Si(OH)_{0.18}(O)_{1.3}$
(600:0.2:100(ethanol))	-	-58.0 (26.3)	-66.3 (73.6)	91	$R'_{0.5}Si(OH)_{0.15}(O)_{1.4}$
BC-d-A(10)	-	-58.0 (11.5)	-67.4 (88.5)	96	$R'_{0.5}Si(OH)_{0.05}(O)_{1.4}$

Figure 2 XRD patterns of the di-amidosils. A: SG-d-A(10) (a), AC-d-A(10) (600:0.2:100(ethanol)) (b), AC-d-A(10) (600:0.2:179(DMSO)) (c) and BC-d-A(10) (d). B: AC-d-A(10) (600:0.2:0) (a), and AC-d-A(10) (600:1:0) (b). The vertical red lines in (B) indicate the kth orders of the lamellar structure found in AC-d-A(10) (600:1:0) and AC-d-A(10) (600:0.2:0) and the blue black thin lines represent the XRD patterns of AC-d-A(10) (600:1:0) and AC-d-A(10) 600:0.2) with magnification (3x) in the 4-12 nm^{-1} region.

J. Mater Chem

ARTICLE TYPE
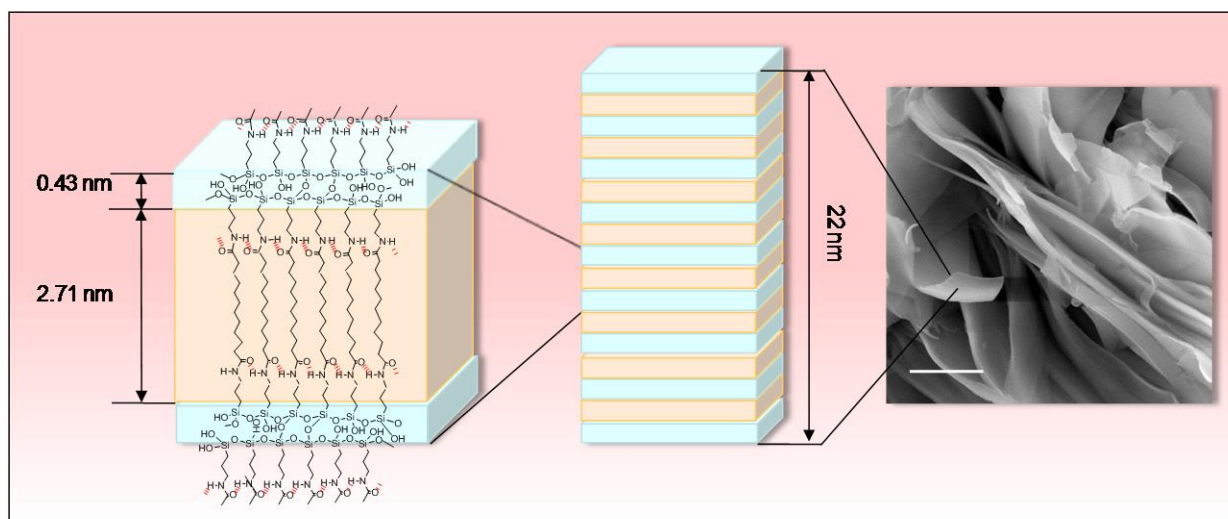
Scheme 2 Schematic representation of the AC-d-A(10) (600:1:0) di-amidosil showing the correspondence of the characteristic dimensions deduced from XRD with those retrieved from SEM data (scale = 2 μm)

2B(a)). The coherence length L, associated with the structural order range of the lamellar structure of the AC-d-A(10) (600:0.2:0) and AC-d-A(10) (600:1:0) samples, was calculated by the Scherrer equation ($L = 2\pi/fwhm$, where fwhm is the full width at half maximum in nm^{-1}) using curve-fitting procedures and assuming Gaussian band shapes. L values of 19 and 22 nm, corresponding to about 7 and 8 lamellae, were obtained, respect-- tively (Scheme 2). The two XRD patterns also show the interparticle contribution at 3.3 nm^{-1} (d_{ip}= 2.0 nm) which is manifested as a shoulder in the case of AC-d-A(10) (600:1:0) (Figure 2B(b)).

Comparison of the high-q region of the XRD patterns of AC-d-A(10) (600:0.2:0) and AC-d-A(10) (600:1:0) (Figure 2B) with that of the amorphous di-amidosils discussed above (Figure 2A) allows inferring that in the former samples the dominating 14.7 nm^{-1} reflection (d_{SiOSi} = 0.43 nm) is better resolved and considerable narrower, a result that denotes a higher degree of structural order. This effect is particularly evident in the case of the AC-d-A(10) (600:0.2:0). In the latter material, the XRD display distinct peaks at: (1) 14.2 nm^{-1} (d_{AA} = 0.44 nm), ascribed to amide-amide spacings[40]; (2) 14.7 nm^{-1} (d_{SiOSi} = 0.42 nm), attributed to ordering within the 2D siloxane domains[39]; (3) 15.1and 15.6 nm^{-1} (shoulder, d_{CCg} = 0.41 and 0.40 nm, respectively), associated with alkyl chains in *gauche* conformations; (4) 16.8, 18.2, 19.2 and 20.8. nm^{-1} (d_{CCt} = 0.37, 0.34, 0.32 and 0.30 nm respectively), attributed to alkyl chains in all-*trans* conformations [41-43] In the case of AC-d-A(10) (600:1:0), three peaks are distinctly seen at 14.2, 14.7 and 15.7 nm^{-1}, whereas in the higher q region only peaks associated with the

occurrence of all-*trans* conformers are detected at 17.9 and 19.9 nm^{-1} (d_{CCt} = 0.35 and 0.32 nm, respectively) (Figure 2B(b)).

Figure 3(a) shows that SG-d-A(10) has a non-porous and homogeneous texture. The morphology of BC-d-A(10) includes smooth spherical objects of variable size, isolated or forming irregular fibres (Figure 3(b)). The AC-d-A(10) (600:1:0) hybrid consists of highly packed platelets of nanometer thickness and micrometer lateral dimensions (Figures 4A(c) and 4A(d) and Scheme 2), assembled in a tight arrangement that reminds the stacking of some seaweeds. Its layered structure, showing some well-ordered features with lamellar spacing, is clearly evident in the TEM and AFM images of AC-d-A(10) (600:1:0) (Figure 5). We note that the interlamellar distance retrieved from the ATM image is consistent with the value retrieved from XRD data. In AC-d-A(10) (600:0.2) the packing of the platelets is globally slightly less compact, giving rise to a morphology that mimics the "desert rose" (Figures 4A(a) and 4A(b)). Interestingly, the texture of AC-d-A(10) (600:0.2) differs markedly from those of the samples synthesized in a similar way but in the presence of a co-solvent. The AC-d-A(10) (600:0.2:179(DMSO)) material comprises leaf-like microplates at the surface of which a few clusters of bounded microparticles of about the same size are attached (Figures 4B(a) and 4B(b)), whereas AC-d-A(10) (600:0.2:100(ethanol)) is composed of interconnected smooth spheres with diameters ranging from 2 to 7 μm (Figures 4B(c) and 4B(d)).
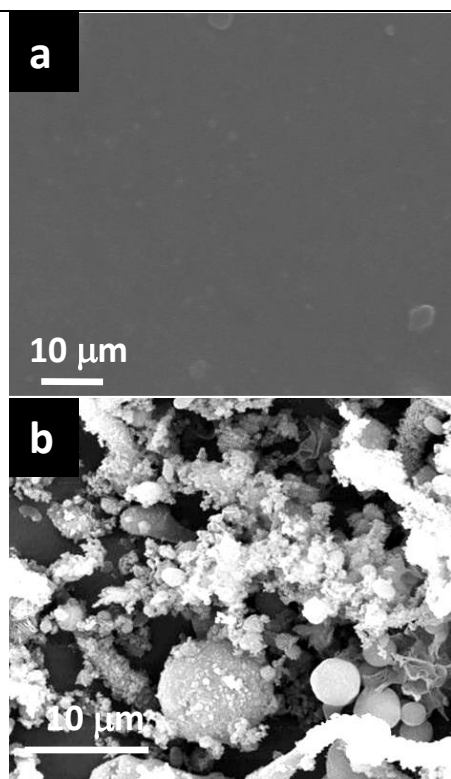
ARTICLE TYPE   www.rsc.org/xxxxxx | XXXXXXXX

Figure 3 SEM images of the SG-d-A(10) (a) and BC-d-A(10) (b) di-amidosils.

The DSC curves of the di-amidosils reproduced in Figure S1 in Supporting Information demonstrate that none of the samples, except BC-d-A(10), AC-d-A(10) (600:0.2:100(ethanol)) and AC-d-A(10) (600:1:0), exhibits any thermal event. Regardless of their degree of order, the three samples mentioned produce a broad endothermic peak centered between 70 and 80 ºC, which is ascribed to the evaporation of the entrapped solvent(s).

To gather additional information on the conformational state of the alkyl chains of the di-amidosils the following diagnostic modes of the hydrocarbon chains were analyzed: the FT-IR and FT-Raman symmetric and asymmetric CH_2 modes (v_sCH_2 and $v_{as}CH_2$, respectively) (3100–2700 cm^{-1} region)[44-50] and the FT-Raman C-C skeletal stretching (vC–C) mode (1140-1040 cm^{-1})[51]. The frequency, fwhm and intensity of these modes have been correlated to the level of ordering of the alkyl chains.[35,44] Typically the FT-IR and FT-Raman v_sCH_2 and $v_{as}CH_2$ bands of crystalline alkyl chains (all-*trans* conformations) are located at lower wavenumbers than those of amorphous alkyl chains (*gauche* conformations)[48-50,52]

The FT-IR spectra of the SG-d-A(10) and BC-d-A(10) di-amidosils in the $v_{as}CH_2$ and v_sCH_2 regions display two strong bands at 2924 cm^{-1} (fwhm = 42 cm^{-1}) and 2853 cm^{-1} (fwhm = 22 cm^{-1}) (black lines in Figure 6A(a) and 6A(b)), respectively), an indication that the alkyl chains adopt *gauche* conformations and are thus amorphous in both hybrids, corroborating the ^{13}C CP/MAS NMR data. The prominent $v_{as}CH_2$ and v_sCH_2 bands at 2916 cm^{-1} (fwhm = 27-25 cm^{-1}) and 2848 cm^{-1} (fwhm = 14-16 cm^{-1}), respectively, found in the FT-IR spectra of AC-d-A(10) (600:0.2:0) and AC-d-A(10) (600:1:0) (red lines in Figure 6A(c) and 6A(f), respectively), characteristic of all-*trans* conformers, confirm the highly crystalline nature of this pair of samples. The
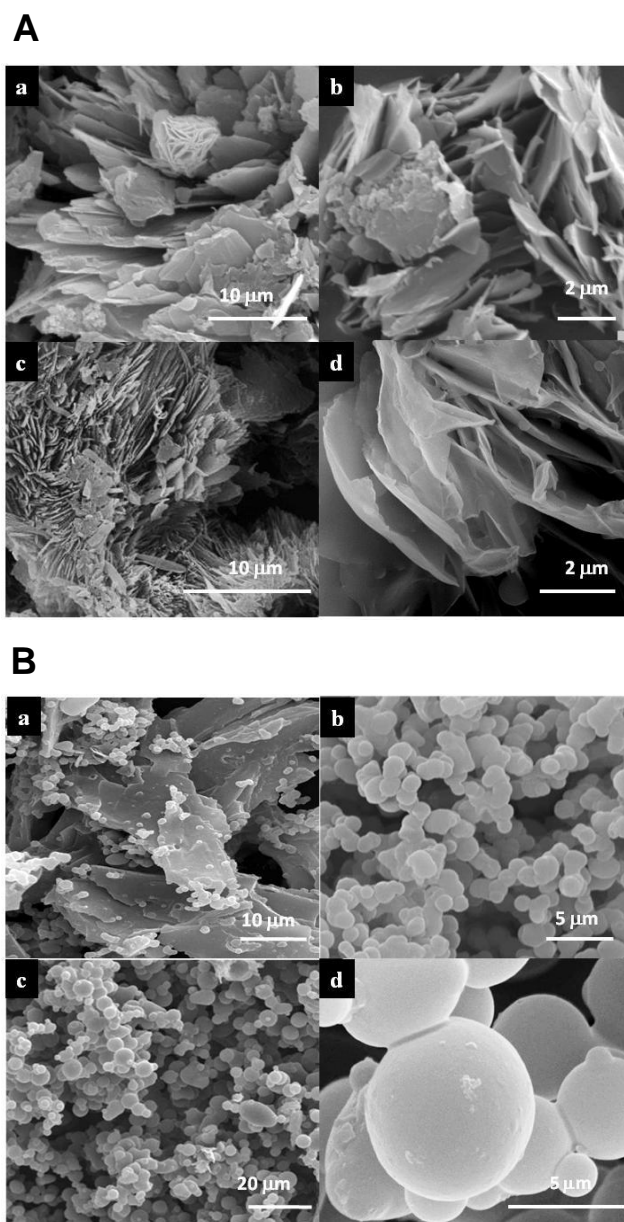

Figure 4 SEM images of the di-amidosils. A. AC-d-A(10) (600:0.2:0) (a and b) and AC-d-A(10) (600:1:0) (c and d); B: AC-d-A(10) (600:0.2:179(DMSO)) (a and b) and AC-d-A(10) (600:0.2:100(ethanol)) (c and d).

shift to higher frequencies and the increase of fwhm undergone by the $v_{as}CH_2$ and the v_sCH_2 bands in the FT-IR spectra of the two samples obtained under the same reaction conditions used to produce AC-d-A(10) (600:0.2:0), but in the presence of ethanol (σ =100) or DMSO (σ = 179) (Figures 6A(d) and 6A(e), respectively), demonstrate that the addition of the co-solvent induced disordering of the alkyl chains. This result is in perfect agreement with the conclusions drawn from ^{13}C CP/MAS NMR data.

The vCH_2 region of the FT-Raman spectrum of SG-d-A(10), AC-d-A(10) (600:0.2:100(ethanol)) and AC-d-A(10) (600:0.2:179(DMSO)) exhibits two broad bands at 2922 and 2891
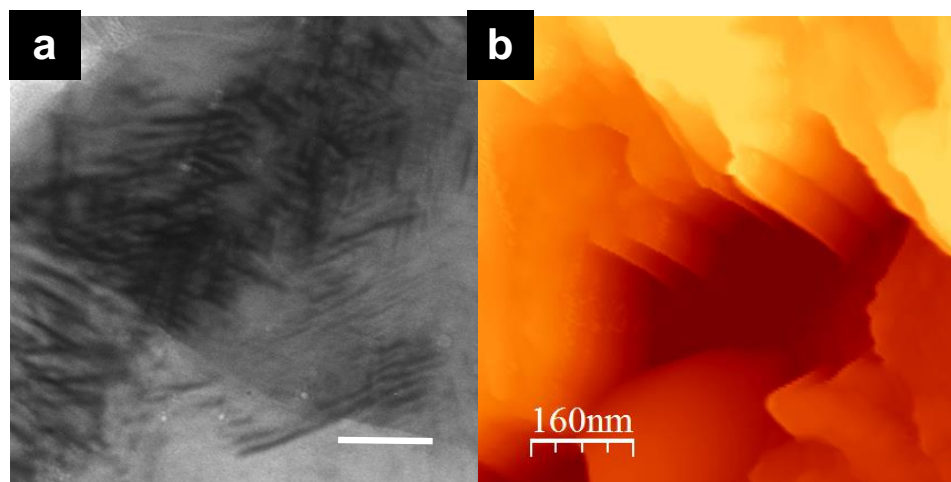
J. Mater Chem

ARTICLE TYPE

Figure 5 TEM (a) and AFM (b) images of the AC-d-A(10) (600:1:0) di-amidosil. Scale in (a): 100 nm.

cm^{-1} and a shoulder at 2852 cm^{-1} (Figure 6B(a), 6B(c) and 6B(d), respectively and Table 2). The band at 2891 cm^{-1} is attributed to $v_{as}CH_2$ mode and the events at 2852 and 2922 cm^{-1} are ascribed to the v_sCH_2 fundamental and to the Fermi resonance between the v_sCH_2 fundamental with the many overtones of the $\square CH_2$ vibrations, respectively. The position and fwhm of these bands in the three hybrids materials are characteristic of alkyl chains in the amorphous state (*gauche* conformations). In the case of AC-d-A(10) (600:0.2:0) and AC-d-A(10) (600:1:0) the FT-Raman $v_{as}CH_2$ mode is downshifted to 2885 cm^{-1} and becomes more intense and sharper (red curves in Figures 6B(b) and 6B(e), and Table 2)), indicating an increase in the proportion of all-*trans* conformers.[47,48] The intensity ratio (*r*) between the FT-Raman v_aCH_2 and v_sCH_2 bands, which is sensitive to the conformational disorder of the alkyl chains and their packing arrangement,[52] was calculated for selected di-amidosils (Table 2). While the *r* value obtained for SG-d-A(10) is of the same order of magnitude of that reported for liquid hexadecane, the value deduced for both AC-d-A(10) (600:0.2:100(ethanol)) and AC-d-A(10) (600:0.2:179(DMSO)) is close to that of liquid cetyl bromide. Samples AC-d-A(10) (600:0.2:0) and AC-d-A(10) (600:1:0) produced values similar to that of solid hexadecane, which yielded the highest value reported by Brown et al.[52]

The FT-Raman $vC–C$ region of AC-d-A(10) (600:0.2:0) and AC-d-A(10) (600:1:0) display bands at 1114, 1101 and 1061 cm^{-1} (red curves in Figures S2(b) and S2(d), respectively). The band at 1114 cm^{-1} (stronger in the case of AC-d-A(10) (600:1:0)) and that 1061 cm^{-1} are attributed to all-*trans* alkyl chains whereas that at 1101 cm^{-1} is assigned to chains with a single *gauche* defect.[53] A shoulder at 1080 cm^{-1} is also discerned in $vC–C$ region, denoting the occurrence of a minor concentration of amorphous alkyl chains.[53]

To elucidate the hydrogen bonding interactions in the di-amidosils the amide I and amide II bands of the FT-IR spectra were analyzed in depth. To determine the individual components of the amide I and amide II envelopes, curve-fitting procedures were performed in the 1750-1500 cm^{-1} interval.

The amide I mode[54] (or C=O stretching mode) is sensitive to the specificity and magnitude of hydrogen bonding. In general it is composed of several distinct components that correspond to different chemical environments (aggregates) of the C=O groups.[55-57] The amide II mode (or N-H in-plane bending mode) is sensitive to chain conformation and intermolecular hydrogen bonding, providing information about the distribution of hydrogen bond strengths.[55] In practice, when the amide group is involved in the formation of hydrogen bonded aggre-gates the amide I band of the "free" amide is downshifted, whereas the amide II band is upshifted.

Figure S3 in Supporting Information demonstrates that the amide I and amide II bands of the SG-d-A(10), BC-d-A(10), AC-d-A(10) (600:0.2:100(ethanol)) and AC-d-A(10) (600:0.2:179(DMSO)) di-amidosils resemble closely. In all these samples the bands are broad and exhibit approximately the same intensity. In contrast, in the case of AC-d-A(10) (600:0.2:0) and AC-d-A(10) (600:1:0) the amide I band is quite sharp and considerably more intense than the amide II band (Figure S3 in Supporting Information). The wavenumber difference ($\Delta\bar{v}$) between both bands provides useful information about the magnitude of the hydrogen bonds. The $\Delta\bar{v}$ value is known to decrease with the increase of hydrogen bond strength. It may be inferred from Figures **7**A(a) and **7**A(b) and Table 3 that in the
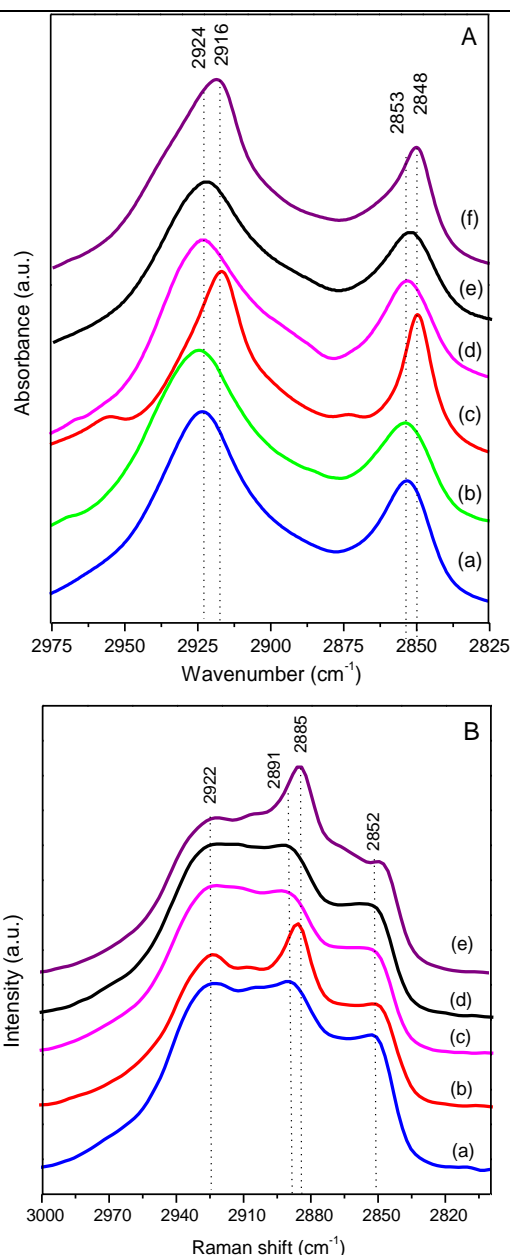
ARTICLE TYPE | www.rsc.org/xxxxxx | XXXXXXXX

Figure 6 $\nu_{as}CH_2$ and $\nu_s CH_2$ regions of the di-amidosils. A: FT-IR spectra of SG-d-A(10) (a), BC-d-A(10) (b), AC-d-A(10) (600:0.2:0) (c), AC-d-A(10) (600:0.2:100(ethanol)) (d), AC-d-A(10) (600:0.2:179(DMSO)) (e) and AC-d-A(10) (600:1:0) (f). B: FT-Raman spectra of SG-d-A(10) (a), AC-d-A(10) (600:0.2:0) (b), AC-d-A(10) (600:0.2:100(ethanol)) (c), AC-d-A(10) (600:0.2:179(DMSO)) (d) and AC-d-A(10) (600:1:0) (e).

case of SG-d-A(10) and BC-d-A(10) the $\Delta\bar{\nu}$ values are 87 and 95 cm^{-1}, respectively. The latter value coincides with that exhibited by m-A(8)[58] (Table 3). For AC-d-A(10) (600:0.2:100(ethanol)), AC-d-A(10) (600:0.2:0) and AC-d-A(10) (600:1:0) the $\Delta\bar{\nu}$ value is the same (89 cm^{-1}) (Figures 7A(c), 7B(a) and 7B(b), respectively) and coincides with that of SG-d-A(10) and with those reported for the mono-amidosils m-A(14)[40] and AC-m-A(8) (1:600)[58] (Table 3). These results suggest that in the present series of di-amidosil materials the weakest hydrogen bond interactions

occur in BC-d-A(10). Globally the strength of the hydrogen-bonded array in the acid-catalyzed di-amidosils has the same magnitude, being as strong as that formed in SG-d-A(10). The $\Delta\bar{\nu}$ value found for AC-d-A(10) (600:0.2:179(DMSO)) (89 cm^{-1}, Figure 7A(d)) is twice higher than that reported earlier (42 cm^{-1}) for a lamellar di-urea cross-linked BS, identified as L12D, also produced in a water/DMSO solution (molar ratio DMSO:water = 527:328) and incorporating alkyl chains of about the same length.[25] This was an expected result, since it is known that the amide group, which contains one hydrogen donor moiety and one hydrogen acceptor moiety, gives rise to considerably weaker hydrogen bonds than the urea group, which comprises two hydrogen donor moieties and one hydrogen acceptor moiety and has an extraordinary self-association ability.

The amide I band of SG-d-A(10), BC-d-A(10) and AC-d-A(10) (600:0.2:179(DMSO)) and AC-d-A(10) (600:0.2:100 (ethanol)) was decomposed into five components at approximately 1733-1726 cm^{-1} (weak (w), fwhm = 13-26 cm^{-1}), 1710-1718 (w, fwhm = 28-14 cm^{-1}), 1656-1650 cm^{-1} (medium (m), fwhm = 22-25 cm^{-1}), 1640-1636 (strong (S), fwhm = 19-33 cm^{-1} and 1623-1617 cm^{-1} (S, fwhm = 25-35 cm^{-1}) (Figure **7**A and Table S2 in Supporting Information). In contrast, the amide I

Table 2 Wavenumber (in cm^{-1}) and intensity ratio r of the FT-Raman $\nu_{as}CH_2$ and $\nu_s CH_2$ bands of selected di-amidosils.

Sample	FT-Raman			
	Fermi Resonance	$\nu_{as}CH_2$	$\nu_s CH_2$	r
SG-d-A(10)	2922	2891	2852	1.33
AC-d-A(10) (600:0.2:0)	2923	2885	2853	1.71
AC-d-A(10) (600:1:0)	2922	2885	2850	1.75
AC-d-A(10) (600:0.2:100(ethanol)	2924	2890	2856	1.46
AC-d-A(10) (600:0.2:179(DMSO)	2922	2891	2854	1.46

band of AC-d-A(10) ((600:0.2:0) and d-A(10) (600:1:0) was resolved into three components situated at 1647 and 1649 cm^{-1} (shoulder (sh), fwhm = 16 and 25 cm^{-1}), 1635 (m, fwhm = 16 and 18 cm^{-1}) and 1620 cm^{-1} (m, fwhm = 22 and 23cm^{-1}) (Figure **7**B and Table S2 in Supporting Information), respectively. The feature around 1733 cm^{-1} is assigned to amide linkages in which the N-H and C=O groups are non-bonded (F).[59] The 1710 and 1656 cm^{-1} components are ascribed to disordered amide-amide aggregates (D1 and D2, respectively, Scheme 3).The 1640 and 1620 cm^{-1} features are attributed to the absorption of C=O groups in ordered amide-amide aggregates (O1 and O2, respectively, Scheme 3) of increasing strength. While the narrowness of the amide I band of AC-d-A(10) (600:0.2:0) and d-A(10) (600:1:0) and the absence of free amide groups in both these two samples (a situation similar to that observed in m-A(14)[40] and AC-m-A(8)(1:600)[58]) reveal that the hydrogen-bonded array is highly directional and embraces all the amide cross-links, the broadness of the amide I band and the presence of non-bonded amide groups

J. Mater Chem

ARTICLE TYPE
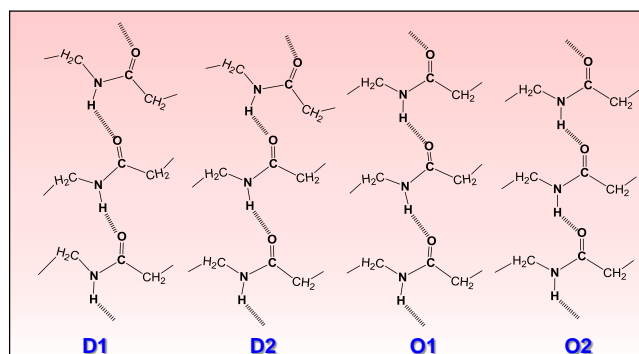
Scheme 3 Tentative representation of the disordered (D) and ordered (O) amide-amide hydrogen-bonded aggregates formed in the di-amidosils.

in the AC-d-A(10) (600:0.2:σ(co-solvent))-based materials prepared in the presence of ethanol and DMSO may be interpreted as an indication that the hydrogen-bonded network is more disordered and does not extend to the entire material. This is also what occurs in m-A(14) after being subject to a heating/cooling cycle [40] and in m-A(8)[58]. The disordering effect caused by the presence of DMSO on the hydrogen bonds was also observed in the case of the L12D material.[25]

The amide II of all the di-amidosils analyzed was decomposed into two components situated approximately at 1562-1555 cm^{-1} (m) and 1543-1537 cm^{-1} (m) (Figure **7** and Table S2 in Supporting Information), suggesting that in all the samples studied hydrogen-bonded aggregates with two distinct degrees of order develop.

On the basis of the set of information retrieved from the above data it is possible at this stage to propose a tentative mechanism to explain the roles of the catalyst and of the co-solvent on the morphology and structure of the di-amidosil samples with respect to those of SG-d-A(10), obtained under classical sol-gel conditions and displaying homogeneous texture and amorphous character.

It is accepted that the production of ordered BS materials relies on the stabilization of amphiphilic organo(bis-silanetriol) structures via the formation of a strong hydrogen-bonded network which in turn induces the organization of the hydrophobic organic spacers.[60] In this type of hybrid systems there is a competitionbetween the formation of hydrogen bonding interactions between silanol (or other) groups and the condensation reactions that yield polysiloxanes. The formation of the ordered organo(bis-silanetriol) structure, which is assisted by the hydrophobic interactions between the organic spacers, is induced under controlled hydrolysis. In this process water plays a key role, promoting the formation of a hydrophilic layer (i. e, the hydrogen-bonded network), while strongly slowing down water producing condensation.
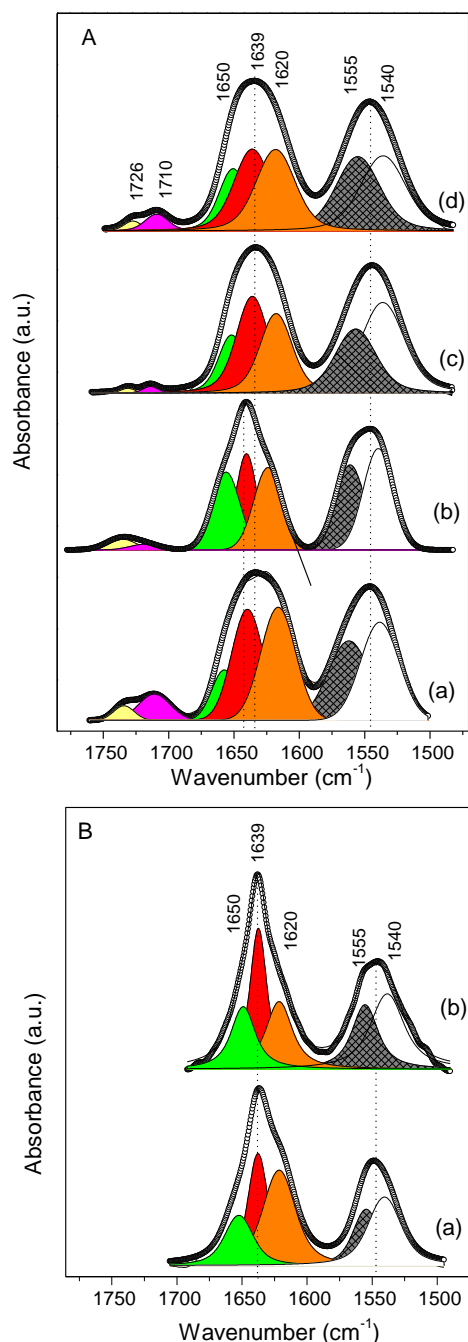

Figure 7 Results of the curve-fitting performed in the FT-IR amide I and amide II regions. A: SG-d-A(10) (a); BC-d-A(10) (b), AC-d-A(10) (600:0.2:100(ethanol)) (c) and AC-d- A(10) (600:0.2:179(DMSO)) (d); B: AC-d-A(10) (600:0.2:0) (a) and AC-d-A(10) (600:1:0) (b).

ARTICLE TYPE www.rsc.org/xxxxxx | XXXXXXXX

The reaction conditions adopted to produce the BC-d-A(10) di-amidosil from the hybrid d-ADPTES(10) precursor (Table S1) resemble closely those typically employed in the sol-gel synthesis of alkoxysilane precursors (Si(OR'')$_4$) catalysed by the hydroxyl (OH$^-$) ion. The OH$^-$-catalyzed hydrolysis is known to occur via an S$_N$2 mechanism in which water first dissociates in a rapid step to produce nucleophilic OH$^-$ ions which then attack the Si atom. Negatively charged pentavalent silicon intermediates are formed and hydrolysis occurs through displacement of an OR''$^-$ ion.[8] With high H$_2$O:Si ratios, in the presence of a basic catalyst and/or at high temperature, the hydrolysis of Si(OR'')$_4$ is significantly faster than condensation, promoting the formation of highly branched compact "colloidal" particle gels.[8] Our results

confirmed that the synthetic conditions used disfavored hydrogen bonding between the amide and/or silanol groups, thus inhibiting the formation of an ordered organo(bis-silanetriol) structure, clearly favoring polycondensation. In BC-d-A(10) the alkyl chains adopt *gauche* conformations and the hydrogen bonding interactions are weaker than those occurring in the other d-A(10)-based materials synthesized (Table 3). As a consequence, the material was produced as an amorphous (Figure 2A(d)) particle xerogel (Figure 3(b)) in which the siloxane network is practically fully polycondensed (c = 96 %, Table 1).

In contrast, the AC-d-A(10) (600:0.2:0) and AC-d-A(10) (600:1:0) di-amidosils were produced under reaction conditions that involved the incorporation of HCl and an amount of water

Table 3 Frequency difference between the intensity maximum of the FT-IR amide I and amide II bands ($\Delta \overline{V}$), average fwhm of the FT-IR O1 and O2 amide I components (fwhmO1/O2), interlamellar distance (*l*) and absolute emission quantum yield (ϕ) (experimental error within 10-25 %) for selected mono- and di-amidosils.

	Sample	$\Delta \overline{V}$ (cm^{-1})	fwhm O1/O2 (cm^{-1})	*l* (nm)	ϕ	λ_{exc} (nm)	Ref.
mono-amidosils	m-A(14)	89	16.0	5.00	0.03	360	40
	m-A(14) heated	104	18.5	4.42	0.072*		
	m-A(8)	97	20.0	-	0.10/0.06	360-380/400	58
	AC-m-A(8) (1:600)	88	24.5	3.38	0.15/0.13	360-380/400	
di-amidosils	d-A(8)	-	31.0	-	0.054/0.034	375/400	31
	SG-d-A(10)	87	29.5	-	0.06/0.09	340/400	This work
	AC-d-A(10) (600:1:0)	89	19.5	2.71	0.17/0.13	360-380/400	
	AC-d-A(10) (600:0.2:0)	89	20.0		0.12/0.09	400/420	
	AC-d-A(10) (600:0.2:100(ethanol))	89	27.5	-	0.07/0.06	320-340/400	
	BC-d-A(10)	95	22.0	-	0.13/0.11	360-380/400	

*After the thermal cycle (heating)

that largely exceeded the values generally used in the case of Si(OR'')$_4$ compounds. These acid-catalyzed samples exhibit lamellar ordered structure (Figures 2B(a) and 2B(b), respectively), a texture that mimics the desert rose (Figures 4A(a) and 4A(b)) and seaweeds (Figures 4A(c) and 4A(d)), respectively, and low *c* values (74 and 72 %, respectively, Table 1). These results demonstrate that in the case of both these samples an ordered organo(bis-silanetriol) structure was indeed preferentially formed, meaning that the formation of hydrogen bonding interactions between the amide and/or silanol groups was definitely favored, unlike polycondensation reactions. The increase of catalyst concentration led to the increase of the all-*trans*/*gauche* conformational ratio (Table 2) and affected morphology slightly. The sol-gel and self-directed assembly processes in AC-d-A(10) (600:0.2:0) and AC-d-A(10) (600:1:0) are thought to have proceeded as follows: (Step 1) Formation of an organo(bis-silanetriol) molecule upon transformation of the ethoxyl groups of d-ADPTES(10) into silanol groups via protonation of each

ethoxyl group in a rapid first step, followed by nucleophilic attack of water molecules from the rear, then formation of a positively charged transition state with significant S$_N$2-type character, and subsequent decay by displacement of ethanol plus inversion of the Si tetrahedron.[8] (Step 2) Formation of hydrogen bonds between amide and/or silanol groups and of van der Waals interactions between alkyl chains directed the assembly of the amphiphilic molecules and induced the growth of ordered organo(bis-silanetriol) structures and ultimately ribbons. (Step 3). Protonation of the growing ribbons due to the low pH of the medium. (Step 4) Further reaction of electrophilic protonated silanol species with d-ADPTES(10) or other silanol species yielded siloxane bonds and allowed the condensation to progress. In water charge mobility was high, charge repulsions were low and the hydrophobic interactions between the alkyl chains were strongly promoted, giving rise to the formation of protonated thin ordered ribbons, with ordered and highly directional hydrogen bonds. These ribbons were subsequently transformed into lamellae, which

J. Mater Chem

ARTICLE TYPE

assembled along a face-to-face fashion, ultimately giving rise to tightly packed crystalline platelets, as shown in the SEM images of Figure 4A. This explanation is perfect agreement with the results described for similar systems by Kuroda et al.[18] who demonstrated that order is associated with weakly condensed layered structures comprising essentially T^2 silicon sites.

Two additional acid-catalyzed samples (AC-d-A(10) (600:0.2:100(ethanol)) and AC-d-A(10) (600:0.2:179(DMSO)) were prepared to elucidate the consequences arising from the introduction of a co-solvent in the reaction medium used to produce AC-d-A(10) (600:0.2:0). While AC-d-A(10) (600:0.2:0) was prepared solely in the presence of water, AC-d-A(10) (600:0.2:100(ethanol)) and AC-d-A(10) (600:0.2:179(DMSO)) were synthesized in aqueous solutions of protic ethanol and aprotic DMSO, respectively. Both solutions were rich in water (molar fractions of 0.143 and 0.298, respectively). These two polar solvents were chosen because they form homogeneous solutions with the d-ADPTES(10) precursor, HCl and water. The presence of ethanol and DMSO during synthesis had dramatic structural consequences, transforming the organized AC-d-A(10) (600:0.2:0) material into two amorphous samples (Figures 2A(b) and 2A(c), respectively) with high c values (91 and 87 %, respectively, Table 1). The morphological implications are also noteworthy: AC-d-A(10) (600:0.2:179(DMSO)) includes leaf-like microplates at the surface of which some disperse clusters of interconnected microparticles emerge (Figures 4B(a) and 4B(b)), whereas AC-d-A(10) (600:0.2:100(ethanol)) is entirely composed of interconnected microparticles (Figures 4B(c) and 4B(d)).

Before attempting to explain how the synthesis of the acid-catalyzed di-amidosils AC-d-A(10) (600:0.2:100(ethanol)) and AC-d-A(10) (600:0.2:179(DMSO)) took place, it is of interest to examine first the physical-chemical properties of the water/ethanol and water/DMSO solutions. Steps (1)-(4) of the mechanism proposed for the ordered AC-d-A(10) (600:0.2:0) and AC-d-A(10) (600:1:0) di-amidosils can be affected by three factors: nucleophilicity of water and silanol species, proton activity and stability of the charged species. These factors are intimately associated with the solvent acceptor number (AN),[61] the solvent basicity (SB)[62] and the solvent dielectric constant (DC). The AN is an index for the strength of the solvent as a Lewis acid. A solvent with low AN increases the nucleophilicity of the oxygen atoms in water or the silanol species, accelerating nucleophilic attack. Upon addition of ethanol ($AN_{ethanol} = 37.1$) and specially DMSO ($AN_{DMSO} = 19.3$), water's AN ($AN_{water} = 54.8$) is lowered, promoting nucleophilic attack. The SB is an index for the hydrogen-bond acceptor basicity of the solvent. A solvent with low SB favors high proton activity, accelerating electrophilic addition of the protons. Because the SB values for ethanol and DMSO are very similar and significantly higher ($SB_{ethanol} = 0.658$ and $SB_{DMSO} = 0.647$) than that of water ($SB_{water} = 0.025$), the addition of these solvents to water results in an

increase of water's SB of about the same order of magnitude, leading to a reduction of the catalytic activity in acidic conditions. The DC is an index for solvent polarity. A solvent with high DC will lead to high stability of the charged species. Adding ethanol ($DC_{ethanol} = 24.55$ (25 ºC)) and DMSO ($DC_{DMSO} = 46.68$ (20 ºC)) to water ($DC_{water} = 80.1$ (20 ºC)) lowers the DC value of the latter. The DC values calculated for the water/ethanol and water/DMSO solutions employed to produce AC-d-A(10) (600:0.2:100(ethanol)) and AC-d-A(10) (600:0.2:179(DMSO)) were 62[63-65]and 71±6[66] respectively, revealing that the charged species formed were considerable less stable in the water/ethanol solution than in the water/DMSO solution.

It is important to recall that in a previous study involving a di-urea cross-linked alkyl/siloxane (a close analogue of the di-amidosil) it was concluded that the replacement of water by a water/DMSO solution rich in DMSO (molar fraction = 0.616) did not affect structurally the resulting material (L12D)[25] which remained lamellar as its parent L12.[21-23] However, upon introduction of DMSO the morphology was changed from rigid platelets (L12[42]) to micro-objects mimicking sea sponges (L12D[25]). Comparison of these results with the present ones leads us to conclude that the structuring of BSs results clearly from a combined effect involving, not only the type of solvent(s) present, but also the nature of the cross-link. The reason for the non-structuring of the AC-d-A(10) (600:0.2:100(ethanol)) and AC-d-A(10) (600:0.2:179(DMSO)) di-amidosils may be found at an early stage of the synthetic mechanism. We believe that although AC-d-A(10) (600:0.2:100(ethanol)) and AC-d-A(10) (600:0.2:179(DMSO)) were prepared in aqueous solutions rich in water, the formation of an ordered organo(bis-silanetriol) structure (Step 2) was not possible partly because of the considerably less self-associating nature of the amide cross-links with respect to the urea cross-links. As a consequence the condensation of the silanol groups with elimination of water (Step 4) proceeded rapidly, yielding disordered materials. In the case of L12D, the significantly less favorable solution medium (rich in DMSO) was counterbalanced by the very directional and strong urea-urea hydrogen bonding interactions formed which prevented any loss of order. The properties of the water/ethanol and water/DMSO solutions account for the morphology exhibited by AC-d-A(10) (600:0.2:100(ethanol)) and AC-d-A(10) (600:0.2:179(DMSO)). In both solutions, but especially in the former one, the acid-catalyzed hydrolysis of d-ADPTES(10) is faster than in water, a situation that favors the formation of highly branched particle gels (Figure 4B). In the water/ethanol solution charge mobility is lower, charge repulsions are higher and the protonated species are less stable than in water solely. These effects are less marked in the water/DMSO solution. The structural effect observed in the water/DMSO and water/ethanol media with respect to the water medium (i. e, total loss of order) is consistent with previous reports that linked the amorphous

ARTICLE TYPE   www.rsc.org/xxxxxx | XXXXXXXX

character of solid networks to the solubilization of the $Si(OR'')_4$ compounds in "good" organic solvents.[67-69]

Let us now examine the photoluminescent features of the di-amidosils. Under UV/visible excitation all the hybrid samples display broad emission spectra between 380 and 680 nm (Figure 8A), whose energy and fwhm depends on the synthetic conditions. The most interesting aspect is related with the appearance of two resolved components peaking at ca. 405/420 nm and 470/520 nm for AC-d-A(10)(600:0.2:0)/BC-d-A(10) (Figure 8A). In previous studies involving analogous hybrid materials, these two emission components, although not resolved in steady-state spectroscopy, were observed in time-resolved emission spectra, being ascribed to electron-hole recombina-tions occurring in the amide cross-links and within the siliceous skeleton, respectively.[31,71-74]

The excitation spectra were selectively monitored within the two emission components around 390 and 480 nm to minimize the spectral overlap, as illustrated in Figure 8B for selected hybrids. These spectra reveal a common component in the UV region around 260 nm and a larger component at high wavelengths between 300 and 420 nm. The peak position and relative intensity of the latter component is strongly dependent on the synthetic conditions. The low- and high- wavelength components preferentially excite the siliceous- and amine-related components, as previously reported.[31,71,73]

The emission of the di-amidosils was quantified through the measurement of the emission quantum yield. The maximum values were measured for AC-d-A(10)(600:0.2:0) (0.13±0.02 excited at 400 nm) and AC-d-A(10)(600:1:0) (0.17±0.02 excited at 360-380 nm) hybrids (Table 3).

The incorporation of ethanol during the synthesis of AC-d-A(10)(600:0.2:ethanol(100)) led to a marked decrease of the quantum yield (0.07±0.01 excited at 320-400 nm) (Table 3). This low value is practically identical (within the experimental error) to that measured for SG-d-A(10) (0.06-0.10 ± 0.01 excited at 340-420 nm) (Table 3). The BC-d-A(10) sample displays a quantum yield of 0.13 ± 0.01 (excited at 360-380 nm) very close to those of AC-d-A(10)(600:0.2:0) and AC-d-A(10)(600:1:0) (Table 3). We note that the maximum value measured for the latter two hybrids exceeds those published for analogous di-ureasil hybrids prepared through the conventional sol-gel route (~0.07-0.09 ± 0.01)[71,72] or the solvolysis method (0.10)[73] being, however, similar to the figures of merit reported for di-urethanesil hybrids prepared via the conventional sol-gel route (0.19)[70] and via acid catalysis (0.20).[73] It is also noteworthy that the maximum value exhibited by SG-d-A(10) (0.10 ± 0.01 excited at 400-420 nm) is ca. three times higher than that previously measured for the analogous d-A(8) di-amidosil containing slightly shorter polymer chains (0.034± 0.01 excited at 400 nm)[31] (Table 3), reinforcing the close relationship existent between the local morphology and the optical features. In the last two years, we emphasized the key role played by the acid catalyst in the enhancement of the emission quantum yield of m-A(8)-based mono-amidosil hybrids[58] and in a new family of tripodal POP/siloxane hybrids (tri-ureasils).[74] For the m-A(8) and AC-m-A(8) (1:600) mono-amidosils maximum and constant quantum yield values of 0.10 ± 0.01 and 0.15±0.01 (excited at 360–380 nm) were measured, respectively (Table 3).[58] For the tri-ureasils maximum and constant quantum yield values of 0.13±0.01 (excited at 360 nm) were achieved for 0.01≤[HCl]≤ 0.1 M.[74]
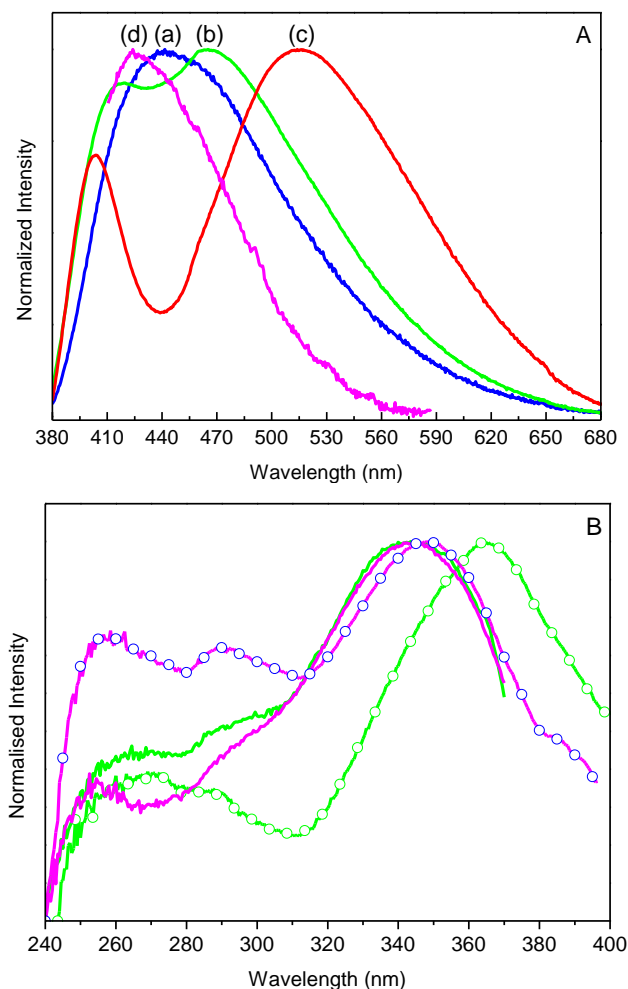

Figure 8 A. Room-temperature emission spectra of the SG-d-A(10) (a), BC-d-A(10) (b), AC-d-A(10)(600:0.2:0) (c) and AC-d-A(10)(600:0.2:ethanol(100)) (d) di-amidosils excited at 360 nm. B. Room-temperature excitation spectra of BC-d-A(10) (green lines) and of AC-d-A(10)(600:0.2:ethanol(100)) (magenta lines) monitored at 390 nm (solid lines) and at 480 nm (solid line and open symbols).

Aiming at gaining further knowledge on the mechanism that governs the optical features of the d-A-(10)-based di-amidosils, steady-state and time-resolved spectroscopy measurements were acquired at 12 K. We restricted this study to the following three samples prepared under completely different reaction conditions: SG-d-A(10), AC-d-A(10)(600:0.2:0) and BC-d-A(10). Their steady state emission and excitation spectra (Figures S4-S6 in Supporting Information) resemble those acquired at room-temperature. Figure 9 shows the time-resolved emission spectra of the three selected hybrids as function of the starting delay (SD) values. For $0.01 \leq SD \leq 4.00$ ms, the spectra are composed of three components peaking at ca. 420 and 465 nm (for all the samples) and between 490 and 510 nm depending on the synthetic route. Upon increasing the SD, only the latter component could be discerned, pointing out a larger time scale behind the emission features, compared to those around 420 and 455 nm. Similar emission components were previously observed for di-ureasils and di-urethanesils,[71,72] for the d-A(8) di-amidosil[31] and for m-A(8)-based mono-amidosils,[58] being ascribed to the contribution

J. Mater Chem

ARTICLE TYPE

from the siliceous (short-lived components at 420 and 450 nm) and amide/amide cross-links (long-lived component at 500 nm). In contrast with the situation found for the siliceous-related component, the energy of the amide-related emission of the di-amidosils depends on the synthetic conditions. In particular, under basic and acid catalysis the emission deviates to the blue relatively to that observed for the hybrid prepared though conventional sol-gel (Figure 9).
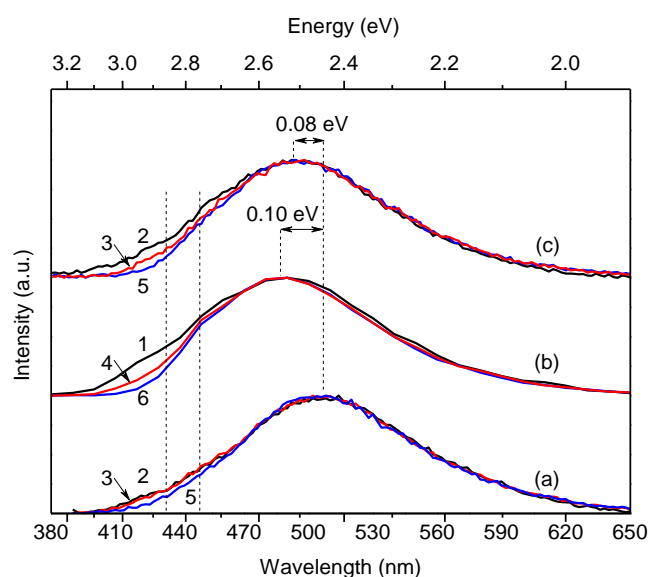

Figure 9. Time-resolved emission spectra (12K) of the SG-d-A(10) (a), BC-d-A(10) (b) and AC-d-A(10)(600:0.2:0) (c) di-amidosils excited at 360 nm and acquired at SD values of 0.01 ms (1), 0.05 ms (2), 4.00 ms (3), 10.00 ms (5) and 12.00 ms (6) .

The emission decay curves were monitored around the emission peak position (490-500 nm, Figures S7-S9 in Supporting Information). The emission decay curves (acquired with SD = 0.05 ms) are well modelled by a bi-exponential function, reflecting the spectral overlap between the siliceous- and amide-related components. The calculated siliceous/amide-related lifetime values were $1.4 \pm 0.1/85.9 \pm 3.8$ ms (AC-d-A(10) (600:0.2:0)), $3.9 \pm 0.4/101.5 \pm 4.4$ ms (SG-d-A(10)), $0.7 \pm 0.1/158.2 \pm 17.2$ ms (BC-d-A(10)). For SG-d-A(10), although a similar value was found for the lifetime of the siliceous component (3.5 ms), a decrease for the amine-related emission was found relatively to the value previously measured for the m-A-(8) mono-amidosil (292 ms).[58] Both lifetime values estimated for AC-d-A(10)(600:0.2:0) are smaller than those previously measured for the AC-d-A-(8) di-amidosil.[58] Concerning the lifetime values measured for BC-d-A(10), while the siliceous-related component is substantially smaller than those of SG-d-A(10) and AC-d-A(10) (600:0.2:0), the lifetime value of the

amine-related component is very close to that of the AC-m-A(8) (1:600) mono-amidosil (156 ms).[58]

The systematic data obtained in the present work, in which we managed to change the structure, morphology and photoluminescence features of several di-amidosils derived from the same hybrid precursor through a fine control of the synthesis conditions, encouraged us to further investigate if, as we suspected, there is a close relationship between the emission quantum yield exhibited by these hybrid materials and the degree of order of the hydrogen-bonded network. With this goal in mind, we decided to calculate the average value of the fwhm of the amide I components corresponding to the ordered hydrogen-bonded amide-amide aggregates O1 and O2 (fwhm O1/O2) (Scheme 3) for each of the d-A(10)-based di-amidosil samples and for the d-A(8) analogue investigated elsewhere.[31] For comparison purposes and also seeking a trend within the mono-amidosil family itself, the fwhm values of m-A(14), m-A(14) after a heating cycle, m-A(8) and AC-m-A(8) (1:600) were also deduced in parallel on the basis of data reported earlier.[40,58]

Figure 10 represents the variation of the emission quantum yield measured at λ_{exc} = 400 nm (to excite the electron-hole recombinations in the amide cross-links) of the d-A(10)-based di-amidosils, and of the d-A(8) di-amidosil and of the mono-amidosils examined in previous works, as a function of the fwhm O1/O2. This plot provides an unprecedented result as it allows discerning two main tendencies in these two classes of amidosils: while in the case of the mono-amidosil hybrids the emission quantum yield increases with the increase of the degree of disorder of the hydrogen-bonded aggregates O1 and O2 (blue ellipse in Figure 10), in the case of di-amidosil materials the reverse tendency is observed (orange ellipse in Figure 10), i.e., the increase of the degree of order of the hydrogen-bonded O1 and O2 array leads to the enhancement of the emission quantum yield. Although it is obvious that the two different trends observed in the amidosils are associated with the presence of a single or two amide cross-links in the chemical structure of the starting hybrid precursor, we cannot provide at present a solid explanation for both behaviors without complementary data involving geometry considerations. For instance theoretical methods have been employed recently to explore the extent to which intermolecular hydrogen bonding can affect the planarity of amide groups in model systems.[75] In the case of the di- and mono-amidosils the geometry of the amide groups and therefore the OCNH dihedral angle in each of the amide-amide aggregates identified is totally unknown. The combination of the information retrieved from Figure 10 and from Table 3 raises, however, several very interesting questions and allows us to draw the following conclusions: (1) Taking into account that in practically all the samples of the two sets of amidosils the strength of the hydrogen-bonded network (measured by $\Delta \bar{\nu}$, cf. Table 3) is globally the same - the only exceptions being m-A(8) and BC-d-A(10) - we
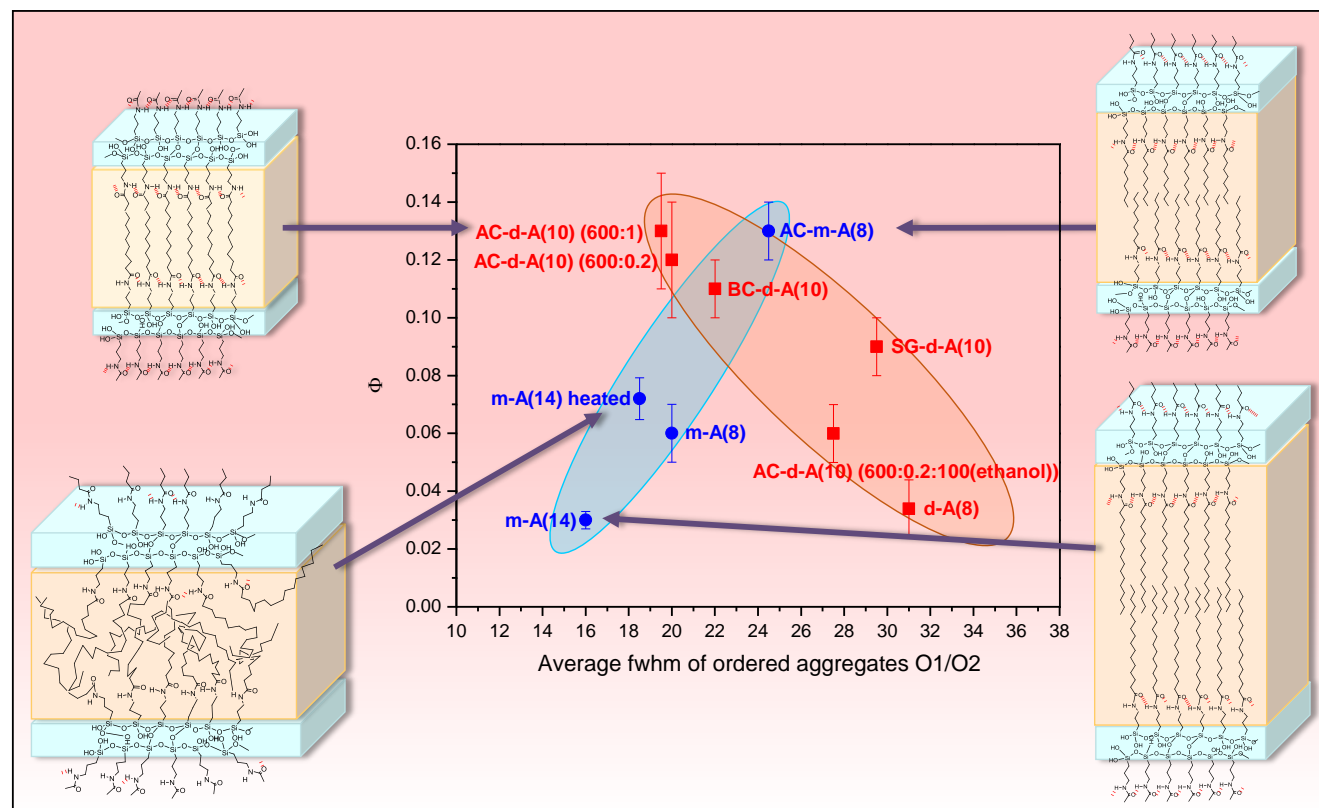
ARTICLE TYPE

Figure 10. Absolute emission quantum yield of the di-amidosils (red symbols) and mono-amidosils (blue symbols) as a function of the average fwhm of the ordered hydrogen-bonded aggregates O1 and O2.

5 are led to conclude that this parameter does not seem to contribute in a significant way to the emission quantum yield value. (2). The huge difference between the emission quantum yield values exhibited by the four amidosil materials devoid of "free" amide groups, i.e., AC-d-A(10) (600:1:0), AC-d-A(10) 10 (600:0.2:0) and AC-m-A(8) (1:600) (0.13, 0.12 and 0.13 ± 0.01, respectively), and m-A(14) (0.030 ± 0.003), suggests that there is apparently no correlation between the extension of hydrogen bonding and the emission quantum yield. (3) In the case of the ordered mono-amidosils displaying lamellar bilayer structure the 15 decrease of the alkyl chain length and the concomitant decrease of l (from 5.00 in m-A(14) to 3.38 nm in AC-m-A(8) (1:600) is accompanied by a marked increase of the emission quantum yield (from 0.030 ± 0.003 to 0.13 ± 0.01, respectively). (4) The lamellar di-amidosils synthesized in the presence of an acid and 20 high water content, AC-d-A(10) (600:1:0) and AC-d-A(10) (600:0.2:0), both with a characteristic l spacing of 2.71 nm, exhibit emission quantum yield values similar to that of the AC-

m-A(8) (1:600) mono-amidosil which was produced under similar experimental conditions. (5) The disordered di-amidosils 25 d-A(8), AC-d-A(10)(600:0.2:ethanol(100)), SG-d-A(10) and BC-d-A(8) exhibit increasing emission quantum yield values in the same order. (6) The emission quantum yield maxima observed in both families of amidosils correspond to samples in which fwhm O1/O2 ranges between 20 and 25 cm⁻¹. The lowest emission 30 quantum yield was measured for the highly ordered m-A(14) and the disordered d-A(8). These samples represent extreme cases in which the fwhm O1/O2 value is the smallest and highest, respectively, of the entire set of amidosils examined. This result may be interpreted as an indication that the hydrogen-bonded 35 amide-amide network in both these materials is too ordered and too disordered, respectively, to promote optimal electron-hole recombination processes in the amide cross-links. It also strongly suggests that, regardless of the degree of order of the amidosil (mono- or di-type), it is the degree of order of the hydrogen-40 bonded amide-amide array that primarily dictates the magnitude

of the emission quantum yield. (7) The acid-catalyzed amidosils (i.e., the ordered AC-d-A(10) (600:1:0) and AC-d-A(10) (600:0.2:0) di-amidosils and the AC-m-A(8) (1:600) mono-amidosil), and the amorphous base-catalyzed di-amidosil BC-d-A(8) are the hybrids which display the highest emission quantum yield values of the whole set of samples examined. This finding supports the claim that, irrespective of the degree of order of the amidosil produced, the addition of an acid or a basic catalyst during synthesis is definitely essential for the production of materials in which the degree of order of the hydrogen-bonded amide-amide array formed falls into the optimal range that favors the highest emission quantum yields.

Conclusions

Di-amide crossed-linked alkyl-based BSs (named di-amidosils and represented by the notation d-A(10)) with tunable structure, morphology and photoluminescente features were produced from the same hybrid precursor by sol-gel reactions and self-assembly routes through a judicious choice of the synthesis conditions. These favored, either the formation of hydrogen bonding interactions between the silanol and/or amide groups of the hydrolyzed precursor and the subsequent growth of an ordered organo(bis-silanetriol) structure, or condensation reactions. An amorphous, non-porous and homogeneous sample (SG-d-A(10)) was produced by the classical sol-gel process. Base catalysis in ethanolic solution and stoichiometric conditions led to the formation of a hybrid (BC-d-A(10)) comprising a fully polycondensed silica network and produced as a mixture of disordered microparticles and irregular fibers. The structuring of the precursor into lamellar materials (AC-d-A(10)(600:1:0) and AC-d-A(10)(600:0.2:0)) was only achieved in the presence of large excess of water and an acid catalyst and in the absence of a co-solvent. At high acid concentration the lamellar stacking resembled seaweeds, whereas low acid content induced a "desert rose"-like texture. Under the latter reaction conditions, but upon addition of a high content of ethanol or DMSO, structuration was inhibited and amorphous microparticles or leaf-like microplates plus some clusters of interconnected microparticles resulted, respectively. The influence of these two solvents on the structure and morphology of the as-derived hybrid compounds was discussed in detail in terms of the physical-chemical properties of the corresponding aqueous solutions using characteristic solvent parameters. The disordered and ordered d-A(10)-based di-amidosils are all room temperature multi-wavelength emitters under UV/VIS excitation. The energy and fwhm of the emission spectra and the peak position and relative intensity of the excitation components depend critically on the synthetic conditions. The highly structured lamellar AC-d-A(10)(600:0.2:0) and AC-d-A(10)(600:1:0) samples and the disordered BC-d-A(10) hybrid exhibited the highest emission quantum yield values of the entire series of di-amidosils studied, demonstrating the interest of adding an acid or a basic catalyst during synthesis. In contrast, the incorporation of ethanol (AC-d-A(10)(600:0.2:ethanol(100)) or the use of classical sol-gel conditions (SG-d-A(10)) was clearly disadvantageous, leading to a marked decrease of the emission quantum yield. The correlation of the emission quantum yield values found for all the di-amidosils and mono-amidosils studied by our group in the last decade with the degree of disorder of the amide-amide hydrogen-bonded array formed in each case, has enabled us to deduce a quantitative relationship reproduced in tendencies of behavior (ellipses in Figure 10) which allow clarifying for the first time the variation of the emission quantum yield in the family of amidosil materials. This correlation provides a simple and fast way of predicting the magnitude of the emission quantum yield prior to measurements, as it requires solely the analysis of the FT-IR amide I band. This insight undoubtedly opens up entirely new perspectives into the field of photoluminescent organic/inorganic hybrid materials incorporating amine cross-links. Work is underway to extend the same approach to the di-ureasils and di-urethanesils extensively investigated by our group.[70]

Acknowledgements

Notes

[a] Chemistry Department and CICS – Health Sciences Research Centre, University of Beira Interior, 6200-001 Covilhã, Portugal.
[b] Chemistry Department, University of Trás-os-Montes e Alto Douro, 5ª000-801 Vila Real, Portugal.
[c] Physics Department and CICECO, University of Aveiro, 3810-193 Aveiro, Portugal.
[d] CQ-VR, University of Trás-os-Montes e Alto Douro, 5001-801 Vila Real, Portugal.

† The manuscript was written through contributions of all authors. / All authors have given approval to the final version of the manuscript. The authors declare no competing financial interest.

‡ Footnotes should appear here. V. de Zea Bermudez: E-mail address: vbermude@utad.pt; Tel: +351-259-350253; Fax: +351-259-350480
S.C.Nunes: E-mail address: snunes@ubi.pt; Tel: +351-275319730; Fax: +351-275 319 730

Electronic Supplementary Information (ESI) available: [Relevant details of the various synthesis conditions used to produce the acid- and base-catalyzed d-A(10)-based di-amidosils. DSC curves of the di-amidosils. FT-Raman spectra of the di-amidosils in the νC-C region. FT-IR spectra of the di-amidosils in the amide I and amide II regions and attribution of the band components. Low-temperature (12 K) emission and excitation spectra of SG-d-A(10), AC-d-A(10)(600:0.2:0) and BC-d-A(10), as function of the excitation and monitoring wavelengths, respectively. Low-temperature (12 K) emission decay curves of SG-d-A(10), AC-d-A(10)(600:0.2:0) and BC-d-A(10), excited at excited at 360 nm and monitored at 500, 495 and 490 nm, respectively].

References

1.   C. Sanchez and P. Gomez Romero, *Functional Hybrid Materials*; Wiley Interscience Eds.: New York, 2003.

2.   G. Kickelbick, *Hybrid Materials: synthesis, characterization and applications*, Wiley-VCH: Weinheim, 2007.

3.   K. J. Shea, D. A. Loy, O. W. Webster, *J. Am. Chem. Soc.*, 1992, **114**, 6700-6710.

4.   K. J. Shea, D. A. Loy, *Chem. Mater.*, 2001, **13**, 3306-3319.

5.   A. Chemtob, L. Ni, C. Croutxé-Barghorn, B. Boury, *Chemistry- A European Journal*, 2014, **20(7),** 1790-1806.

6.   C. Sanchez, B. Julian, P. Belleville, M. Popall, *J. Mater. Chem.,* 2005, **15**, 3559-3592.

7.   S. Sanchez, P. Belleville, M. Popall, L. Nicole, *Chem. Soc. Rev.,* 2011, **40**, 696-753.

8.   J. Brinker, G. W. Scherer, *Sol-gel Science: The Physics and Chemistry of Sol-Gel Processing*, Academic Press: San Diego, CA, 1990.

9.   S. Mann, S.-L. Burkett, S. A. Davis, C. E. Fowler, N. H. Mendelson, S. D. Sims, D. Walsh, N. T. Whilton, *Chem. Mater.,* 1997, **9**, 2300-2310.

10.   C. T: Kresge, M. E. Leonowicz, W. J. Roth, J. C. Vartulli, J. S. Beck, *Nature,* 1992, **359**, 710-712.

11.   Y. Lu, R. Ganguli, C. A. Drewien, M. T. Anderson, C. J. Brinker, W. Gong, Y. Guo, H. Soyez, B. Dunn, M. H. Huang, J. I. Zink, *Nature*, 1997, **389**, 364-368.

12.   C. J. Brinker, Y. F. Lu., A. Sellinger, H. Y. Fan, *Adv. Mater.,* 1999, **11**, 579-585.

13.   S. Fujita, S. Inagaki, *Chem. Mater.,* 2008, **20**, 891-908.

14.   Y. Lu, H. Fan, N. Doke, D. A. Loy, R. A. Assink, . D. A. LaVan, C. J. Brinker, *J. Am. Chem. Soc.,* 2000, **122 (22)**, 5258-5261.

15.   G. A. Ozin, *Chem. Commun.*, 2000, 419-432.

16.   K. J. C. Van Hommel, A. Friggeri, S. Shinkai, *Angew Chem. Int. Ed.,* 2003, **42**, 980-999.

17.   J. Alauzun, A. Mehdi, C. Reyé, R. J. P. Corriu, *J. Mater. Chem.,* 2005, **15**, 841-843.

18.   A. Shimojima, Y. Sugahara, K. Kuroda, *Bull. Chem. Soc. Jpn.,* 1997, **70**, 2847.

19.   Y. Fujimoto, A. Shimojima, K. Kuroda, *Chem. Mater.,* 2003, **15**, 4768-4774.

20.   A. Shimojima, K. Kuroda, *Angew. Chem. Int. Ed.,* 2003, **42**, 4057-4060.

21.   J. J. E. Moreau, L. Vellutini, M. Wong Chi Man, C. Bied, J.-L. Bantignies, P. Dieudonné, J.-L. Sauvajol, *J. Am. Chem. Soc.*, 2001, **123,** 7957-7958.

22.   J. J. E. Moreau, L. Vellutini, M. Wong Chi Man, C. Bied, *Chem Eur J.,* 2003, **9**, 1594-1599.

23.   J. J. E. Moreau, L. Vellutini, P. Dieudonne, M. Wong Chi Man, J.-L. Bantignies, Sauvajol, C. Bied, *J. Mater. Chem.* 2005, **15**, 4943-448.

24.   X. Zhou, S. Yang, C. Yu, Z. Li, X. Yan, Y.Cao, D. Zhao, *Chem. Eur. J.,* 2006, **12**, 8484-8490.

25.   M. Fernandes, X. Cattoën, M. Wong Chi Man, V. de Zea Bermudez, *Cryst. Eng. Commun.,* **2011**, *123*, 1410-1415.

26.   M. Fernandes, S. S. Nobre, X. Qinghong, C. Carcel, J. N. Cachia, X. Cattoën, J. M. Sousa, R. A. S. Ferreira, L. D. Carlos, C. V. Santilli, M. Wong Chi Man, V. de Zea Bermudez, *J. Phys. Chem. B*, 2011, **115**, 10877-10891.

27.   N. Liu, K. Yu, B: Smarsly, D. R. Dunphy, Y. Jiang, C. J. Brinker, *J. Am. Chem. Soc.*, 2002, **124**, 14540-14541.

28.   K. Okamoto, Y. Goto, S. Inagaki, *J. Mater. Chem.*, 2005, **15**, 4136-4140.

29.   J. J. E. Moreau, B. P. Pichon, M. Wong Chi Man, C. Bied, H. Pritzkow, J.-L. Bantignies, P. Dieudonné, J.-L. Sauvajol, *Angew. Chem. Int. Ed.,* 2004, **43**, 203-206.

30.   J. J. E. Moreau, L. Vellutini, M. Wong Chi Man, C. Bied, *J. Am. Chem. Soc.*, 2001, **123**, 1509-1510.

31.   S. C. Nunes, V. de Zea Bermudez, J. Cybinska, R. A. S. Ferreira, J. Legendziewicz, L. D. Carlos, M. M. Silva, M. J. Smith, D. Ostrovskii, J. Rocha, *J. Mater Chem*, 2005, **15**, 3876-3886.

32.   I. Horcas; R. Fernandez, J. M. Gomez-Rodriguez, J. Colchero, J. Gomez-Herrero, A. M. Baro, *Rev. Sci. Instrum.,* 2007, **78**, 13705-13708.

33.   Peakfit is a product of Jandel Corporation, 2591 Rerner Boulevard, San Rafael, CA 94901, U.S.A.

34.   J. Clauss, K. Schmidt-Rohr, A. Adam, C. Boeffel, H. W.; Spiess, *Macromolecules,* 1992, **25**, 5208-5214.

35.   A. N. Parikh, M. A. Schivley, E. Koo, K. Seshadri, D. Aurentz, K. Mueller, D. L. Allara, *J. Am. Chem. Soc.*, 1997, **119**, 3135-3143.

36.   L.-Q. Wang, J. Liu, G. J. Exarhos, K. Y. Flaniga, R. Bordia, J. Phys. Chem. B, 2000, **104**, 2810-2816.

37.   S. Monredon, C. Bonhomme, F. Ribot, F. Babonneau, *J. Sol-Gel. Sci. Technol.*, 2009, **50**, 152-157.

38.   E. Ruiz-Hitzky, H. Ariga, Y. Lvov, Bio-inorganic Hybrid Materials – Strategies, Syntheses, Characterization and Applications, John Wiley &Sons, 2008.

39.   L. D. Carlos, V. de Zea Bermudez, R. A. S. Ferreira, L. Marques, M. Assunção, *Chem. Mater.*, 1999, **11(3)**, 581-588.

40.   L. D. Carlos, V. de Zea Bermudez, V. S. Amaral, S. C. Nunes, N. J: O. Silva, R. A. S. Ferreira, C. V. Santilli, D. Ostrovskii, J. Rocha, *Adv. Mater.,* 2007, **19**, 341-348.

41.   C. Boehm, F. Leveiller, D. Jacquemain, H. Mohwald, K. Kjaer, J. Als-Nielsen, I. Weissbuch, L. Leiserowitz, *Langmuir*, 1994, **10**, 830-836.

42.   M. Fernandes, R. A. S. Ferreira, X. Cattoën, L. D. Carlos, M. Wong Chi Man, V. de Zea Bermudez, *J. Sol-Gel. Sci. Technol.*, 2012, DOI 10.1007/s10971-012-2739-1.

43.   S. S. Nobre, C. D: S. Brites, R. A.S. Ferreira, V. de Zea Bermudez, C. Carcel, J. J. E. Moreau, J. Rocha, M. Wong Chi Man, L. D. Carlos, *J. Mater. Chem.*, 2008, **18**, 4172-4182.

44.   R. G. Snyder, H. L. Strauss, C. A. Ellinger, *J. Phys. Chem.,* 1982, **86**, 5145-5150.

45.   R. A. Macphail, H. L. Strauss, R. G. Snyder, C. A. Ellinger, *J. Phys. Chem.*, 1984, **88**, 334-341.

46.   M. D. Porter, T. B. Bright, D. L. Allara, C. E. D. Childsey, *J. Am. Chem Soc.*, 1987, **109**, 3559-3568.

47.   R. Wang, G. Baran, S. L. Wunder, *Langmuir*, 2000, **16**, 6298-6305.

48.   N. V. Venkataram, S. Vasudevan, *J. Phys. Chem. B*, 2001, **105**, 7639-7650.

49.   N. V. Venkataram, S. Bhagyalakshmi, S. Vasudevan, R. Seshachi, *Phys. Chem. Chem. Phys.*, 2002, **4**, 4533-4538.

50.   S. Singh, J. Wegmann, K. Albert, K. Muller, *J. Phys. Chem. B,* 2002, **106**, 878-883.

51.   F. Bensebaa, Y. Zhou, A. G. Broto, D. E. Irish, Y. Deslandes, E. Kruss, T. H. Ellis, Spectrochimica Acta Part A, 1999, 55, 1229-1236.

52.   K. G. Brown, E. Bicknell-Brown, M. Ladjadj, *J. Phys. Chem.,* 1987, **91**, 3436-3442.

53.   R. J. Meier, A. Csiszar, E. Klumpp, *Journal of Phys Chem*. B, 2006, **110(12)**, 5842-5844.

54.   T. Miyazawa, T. Shimanouchi, S.-I. Mizushima, *J. Chem. Phys*., 1956, **24 (2),** 408-418.

55.   D. J. Skrovanek, S. E. Howe, P. C. Painter, M. M. Coleman, *Macromolecules*, 1985, **18**, 1676-1683.

56.   D. J. Skrovanek, P. C. Painter, M. M. Coleman, *Macromolecules,* 1986, **19**, 699-705.

57.   M. M. Coleman, K. H. Lee, D. J. Skrovanek, P. C. Painter, *Macromolecules*, 1986, **19**, 2149-2157.

58.   S. C. Nunes, N. J. O. Silva, J. Hümmer, R. A. S. Ferreira, P. Almeida, L. D. Carlos, V. de Zea Bermudez, *RSC Advances*, 2012, **2**, 2087-2099.

59.   H. Matsuura, T. Miyazawa, K. Machida, *Spectrochim. Acta*, 1973, **29A**, 771-779.

60.   G. Cerveau, R. J. P. Corriu, B. Dabiens, J. Le Bideau, *Angew. Chem. Int. Ed.*, 2000, **39**, 4533-4537.

61.   W. B. Jensen, *Chem. Rev.*, 1978, **78**, 1-22.

62.   J. Catalán, in Handbook of Solvents, G. Wypych Ed.: 2001, ChemTec Publishing, Toronto, Canada, pg. 583-616.

63.   S. J. Suresh, V. M. Naik, *J. Chem. Phys* ,2002, **116**, 4212-4220.

64.   H. Yilmaz, *Turk. J. Phys.,* 2002, **26**, 243-246.

65.   M. Faraday, *Journal of Applied Chemical Research*, 2012, **20(1),** 28-35.

66.   J. Catalán, C. Díaz, F. García-Blanco, *J. Org. Chem*., 2001, **66**, 5846-5852.

67.   E. Z. Faraggi, Y. Sorek, O. Levi, Y. Avny, D. Davidov, R. Neumann, R. Reisfield, *Adv. Mater.,* 1996, **8**, 833-837.

68.   Dautel, O. J.; Lere-Porte, J.-P.; Moreau, J. J. E.; Wong Chi Man, M. *Chem. Commun.,* 2003, 2662-2663.

69.   S. Bourg, J.-C. Broudic, O. Conocar, J. J. E. Moreau, D. Meyer, Wong Chi Man, M. *J. Mater. Chem.*, 2001, **11**, 491-511.

70.   L. D. Carlos, L. D.; Ferreira, R. A. S.; de Zea Bermudez, V.; Ribeiro, S. J. L. *Adv. Funct. Mater.*, 2001, **11**, 111-115.

71.   L. D. Carlos, R. A. S. Ferreira, R. N. Pereira, M. Assunção, V. de Zea Bermudez *J. Phys. Chem. B,* 2004, **108**, 14924-14932.

72.   S. S. Nobre, P. P. Lima, R. A. S. Ferreira, R. O. Freire, L. Fu, U. Pischel, V. de Zea Bermudez, O. L. Malta, L. D. Carlos, *J. Phys. Chem. C,* 2007, **111**, 3275-3284.

73.   L. Fu, R. A. S. Ferreira, N. J. O. Silva , L. D. Carlos, V. de Zea Bermudez, J. Rocha, *Chem. Mater.,* 2004, **16**, 1507-1516.

74.   V. T. Freitas, P. P. Lima, V. de Zea Bermudez, R. A. S. Ferreira, L. D. Carlos, *Eur. J. Inorg. Chem.*, 2012, 5390-5295.

75.   J. A. Platts, H. Maarof, K. D. M. Harris, G. K. Lim, D. J. Willock, *Phys. Chem. Chem. Phys.*, 2012, **14**, 11944-11952.

TOC

Di-amidosils with Tunable Structure, Morphology and Emission Quantum Yield: The Role of Hydrogen Bonding.

S. C. Nunes,[*] J. Hümmer, V. T. Freitas, R. A. S. Ferreira, L. D. Carlos, P. Almeida, V. de Zea Bermudez[*]

Di-amidosil hybrids with variable structure, morphology and photoluminescence properties were synthesized from the same precursor via sol-gel reactions and self-assembly routes using different experimental conditions. Lamellar structures were only produced at high water content and with an acid catalyst. This structuring was suppressed upon addition of a co-solvent. The maximum absolute emission quantum yield value (ca. 013 $\pm$ 0.01 at λ_{exc} = 400 nm) was measured for the samples obtained in the presence of a catalyst (acid or base). Comparison of the results derived from this work with previous data on di- and mono-amidosils, allowed us proposing an easy way of predicting the magnitude of the emission quantum yield of the amidosil hybrids based merely on the calculation of the degree of order of the amide-amide hydrogen-bonded array.

Tunable structure/morphology/photoluminescence features